NUREG/CR-3366
SAND83-1350
R7
Printed April 1984

High Temperature Melt Attack on Steel and Urania-Coated Steel

D. A. Powers, F. E. Arellano

Prepared by
Sandia National Laboratories
Albuquerque, New Mexico 87185 and Livermore, California 94550
for the United States Department of Energy
under Contract DE-AC04-76DP00789

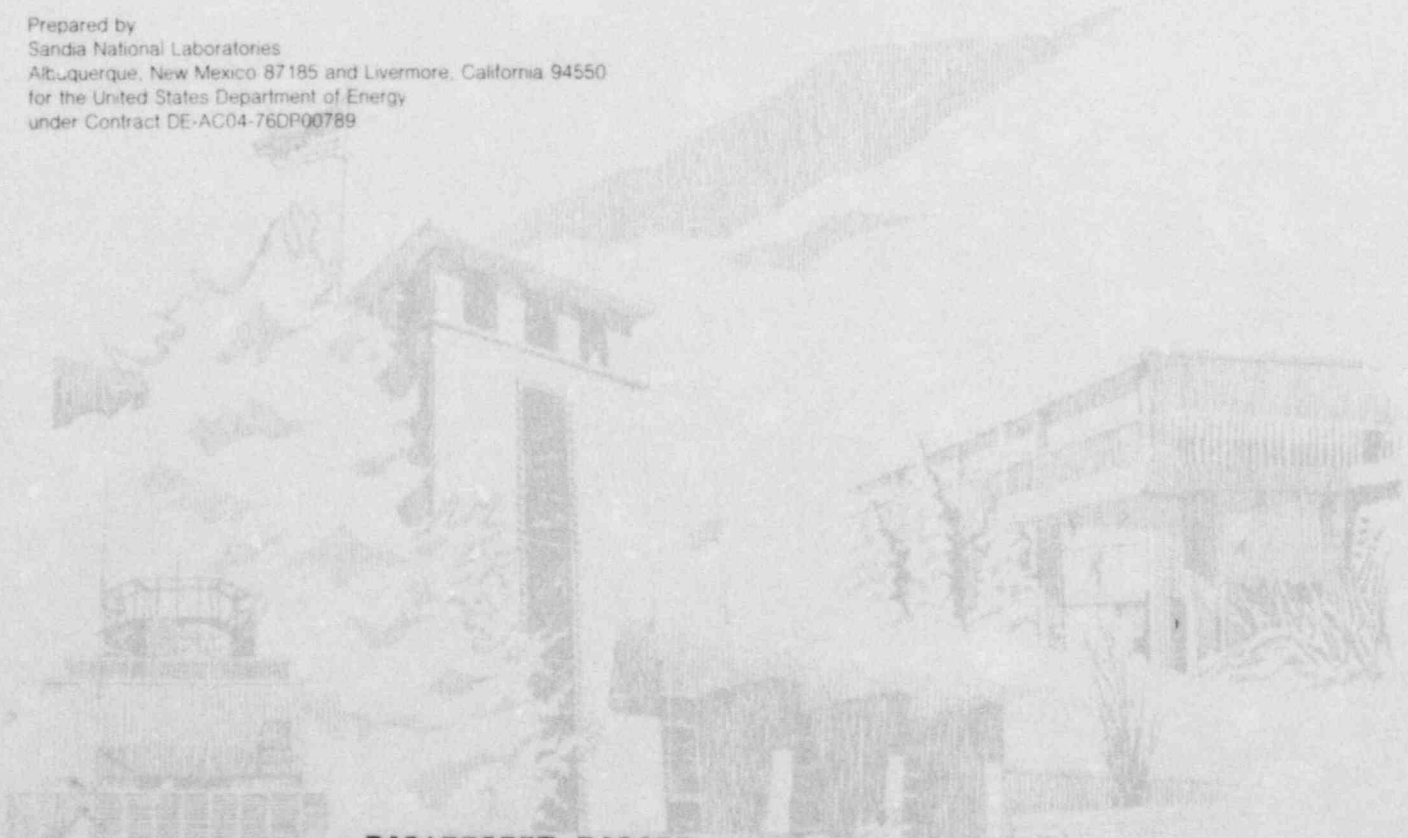

Prepared for
U. S. NUCLEAR REGULATORY COMMISSION

Available from

GPO Sales Program
Division of Technical Information and Document Control
U.S. Nuclear Regulatory Commission
Washington, D.C. 20555

and

National Technical Information Service
Springfield, Virginia 22161

NUREG/CR-3366
SAND83-1350
R7

HIGH TEMPERATURE MELT ATTACK ON STEEL AND URANIA-COATED STEEL

L. A. Powers and F. E. Arellano

Date Published:
April 1984

Sandia National Laboratories
Albuquerque, New Mexico 87185
operated by
Sandia Corporation
for the
U.S. Department of Energy

Prepared for
Division of Reactor Safety Research
Office of Nuclear Regulatory Research
U.S. Nuclear Regulatory Commission
Washington, DC 20555
Under Memorandum of Understanding DOE 40-550-75
NRC FIN No. A1247

ABSTRACT

A series of twelve experiments in which high-temperature melts streamed onto steel plates are described. Melts weighing 3 to 5 kg were formed by metallothermic reaction and had the compositions 55 w/o Fe and 45 w/o Al_2O_3 or 54 w/o UO_2, 16 w/o ZrO_2 and 30 w/o stainless steel. Steel plates exposed to the melts were between 0.95 and 1.90 cm thick. Some plates were coated with plasma-sprayed urania to thicknesses up to 2 mm. Stream velocities were varied between 102 and 255 cm/s.

Steel plates exposed to the direct action of the melts were readily penetrated. Typical penetration rates were about 1 cm/s. The rate of penetration increased with the velocity of the melt stream. Urania coatings 0.23 and 1.0 mm thick inhibited penetration of the steel. Coatings 2 mm thick prevented penetration of plates exposed to melt for about 5 seconds.

Data obtained in these tests and previous tests were used to form a correlation of the time, t (s), required to penetrate a steel plate of thickness d in terms of melt temperature, T_m (K), and melt velocity, V (cm/s),:

$$t = \frac{(4.518 \pm 0.103)\ \rho d Q\ V^{-1/2}}{(T_m - T_b)}$$

where ρ (g/cm^3) is the density of the plate, Q (cal/gm) is the heat of ablation, and T_b (K) is the plate ablation temperature. It was unnecessary to include stream diameter to obtain a satisfactory correlation.

TABLE OF CONTENTS

		Page
I)	Introduction and Motivation for the Experiments	1
II)	Description of the Experiments	2
III)	Results	14
	A) Events of the Tests	14
	B) Impact Velocities of the Melts	17
	C) Perforation of Plates	20
	D) Empirical Correlation of the Test Results	25
	E) Effects of Urania Coatings	32
IV)	Global Correlation of Penetration Data	37
V)	References	51
VI)	Appendices	
	A) Maximum Temperatures During Corium Metallothermic Reactions	53
	B) Temperature Data from the PLATE tests	62
	C) Description of Inverse Heat Flux Analysis	75

ILLUSTRATIONS

Figure		Page
1	Cross-Sectional Side View of the Apparatus	3
2	Top View of the Apparatus	4
3	Photographs of the Apparatus Used in Tests PLATE #6 and PLATE #8	5
4	Temperature History of a Copper Melt Plug	7
5	Photographs of the Urania Coating Used in Test PLATE #15	10
6	Example of Thermocouples Attached to the Bottom of a Steel Plate to be Exposed to Melt	13
7	Test PLATE #11 Just After Melt Penetrated the 1.9 cm Steel Plate	16
8	Melt Velocity as a Function of the Distance from the Melt Plug	18
9	Penetrations Produced in Tests PLATE #5 and PLATE #6	21
10	Penetrations Produced in Tests PLATE #7 and PLATE #8	22
11	Penetrations Produced in Tests PLATE #10 and PLATE #11	23
12	Penetration Produced in Tests PLATE #12 and PLATE #20	24
13	Plot of Penetration Diameter Against the Square Root of the Melt Velocity at Impact	26
14	Time Required for Melt to Penetrate Plates of Various Thicknesses	28
15	Penetration of Plates by Melts of Various Velocities	30
16	Reciprocal of the Delay Time Caused by Urania Coatings 0.23 to 2 mm Thick	33

ILLUSTRATIONS Continued

Figure		Page
17	Heat Flux to the Steel in Test PLATE #15 Calculated by Inverse Heat Flux Analysis	34
18	Heat Flux to the Steel in Test PLATE #17 Calculated by Inverse Heat Flux Analysis	35
19	Time Required to Penetrate Steel Plates of Various Thicknesses by 2000°C Melts that Impact the Plates at 250 cm/s	47
20	Time Required to Penetrate a 10 cm Thick Steel Plate by a 2000°C Melt that Impacts the Plate at Various Velocities	48
21	Time Required to Penetrate a 10 cm Thick Steel Plate by Melts of Various Temperatures that Impact the Plate at 250 cm/s	49
A-1	Effect of Contamination or Incomplete Reaction on the Maximum Temperature of "Corium" Metallothermic Reactions	61
B-1	Temperature Data from Test PLATE #5	63
B-2	Temperature Data from Test PLATE #6	64
B-3	Temperature Data from Test PLATE #7	65
B-4	Temperature Data from Test PLATE #8	66
B-5	Temperature Data from Test PLATE #10	67
B-6	Temperature Data from Test PLATE #11	68
B-7	Temperature Data from Test PLATE #12	69
B-8	Temperature Data from Test PLATE #14	70
B-9	Temperature Data from Test PLATE #15	71
B-10	Temperature Data from Test PLATE #16	72
B-11	Temperature Data from Test PLATE #17	73

ILLUSTRATIONS Continued

Figure		Page
B-12	Temperature Data from Test PLATE #20	74
C-1	Calculated Heat Flux Based on "Noisy", "Filtered" Data	79
C-2	Time Dependence of the Relative Temperature Error Associated with the One-Dimensional Approximation	83

TABLES

Number		Page
I	X-ray Powder Diffraction Data for Urania Coatings	9
II	Constituents of the Corium Reaction Mixture	11
III	Summary of the Experiments	15
IV	Summary of Data from the Tests	19
V	Data Used to Develop the Correlation	40
VI	Results of Least-Square Fittings	42
VII	Comparison of Calculated and Observed Penetration Times	43
A-1	Constituents of the Corium Metallothermic Reaction Mixture	54
A-2	Parameters for the Temperature Rise Calculations	57
A-3	Vaporization of Metals	59
C-1	Comparison of Calculated and Actual Surface Heat Fluxes	78

I. INTRODUCTION AND MOTIVATION FOR THE EXPERIMENTS

Erosion of steel structures by high temperature melts plays an important role in the analysis of core meltdown during severe reactor accidents. Penetration of the reactor vessel by melt and penetration of the steel reactor cavity liner prior to the onset of melt interactions with concrete are obvious examples of how melt erosion of steel affects the timing of events in reactor accidents. Most considerations of the erosion process in the past have focused on steel erosion by molten reactor fuel. It is likely, however, that molten metals will be more aggressive penetrators of steel structures in a reactor.

In a previous work (1) the aggressive attack on steel structures by molten stainless steel at 1700^{o}C was described. This work showed that melt velocity was very important in determining how rapidly steel structures could be penetrated.

The work described here extends these previous studies to include higher temperature melts (2700 to 3060 K) and melts of the prototypic "corium" composition. These studies attempt to show the magnitude of the heat flux imposed on steel structures by flowing melts. The variation in this heat flux with melt velocity is an important aspect of this work.

For some reactor accidents, it has been hypothesized that critical steel structures might be exposed to small urania melts prior to being subjected to intense heat fluxes produced when in contact with bulk core melt. In these cases the steel structure would be coated with thin layers of quenched urania which, it is supposed, might protect the steel and delay substantially penetration of the steel by bulk melt. The effectiveness of such thin layers of urania in protecting steel from melt attack was also addressed in this work.

Finally, an attempt has been made to correlate empirically results of tests described here and the previous results into a correlation that can be used for computer analyses of reactor accidents.

II. DESCRIPTION OF THE EXPERIMENTS

The procedure used in the experiments began with the generation of a high-temperature melt by a metallothermic reaction within a refractory crucible. Once the melt was formed it would dissolve a plug at the bottom of the crucible and stream onto a flat plate of the chosen material for the interaction experiment. Schematic diagrams of the experimental apparatus are shown in Figures 1 and 2. Photographs of the apparatus for two tests are shown in Figure 3.

The refractory crucibles used in the tests were made of fireclay. This material has a melting point well below the reaction temperatures generated during the melt-forming processes. The melts were within the crucible for such short periods of time (typically about 10 seconds) that ablation of the crucible proved to be no problem. Usually less than 0.1 cm of the crucible wall material would erode during a test.

The crucibles were always fractured, probably by thermal shock, during a test. For this reason the crucibles were wrapped with layers of formable asbestos paper to a thickness of about 0.8 cm. In some tests the crucible was further protected by embedding it in a magnesia dry ram held within a 31 cm diameter pipe. In no case was it observed that melt flowed into cracks in the crucibles. After the tests the entire inside surface of the crucible cavity was found to be coated with a layer of quenched oxide melt about 0.1 cm thick.

The crucibles had a capacity of about 1.2 liters. They were tapered slightly from top to bottom. The maximum inside diameter was 12.7 cm. At the bottom, the crucible cavity was about 5.8 cm in diameter. The inside height of the crucible cavity was 17.8 cm. Charge materials filled the cavity to within about 1 cm of the top. At the completion of the reaction, the top of the melt was about 8 cm below the top of the cavity.

The crucible walls were about 1.3 cm thick. The base of the crucible was about 1.9 cm thick. A hole, 1.3 cm in diameter, was drilled in the bottom of the crucibles. A countersink, 2 cm in diameter and 0.9 cm deep, was drilled inside the crucible. This countersink provided a seat for a copper melt plug 1.9 cm in diameter and 0.12 cm thick. Once the metallothermic reaction that formed the melt was complete, this copper plug was quickly melted and the melt could stream from the crucible onto the target plate. A typical temperature history of a copper plug obtained from a type K thermocouple welded to the backside of the plug is shown in Figure 4. The zero time for this history was arbitrarily selected. The history shows that the melting of the plug

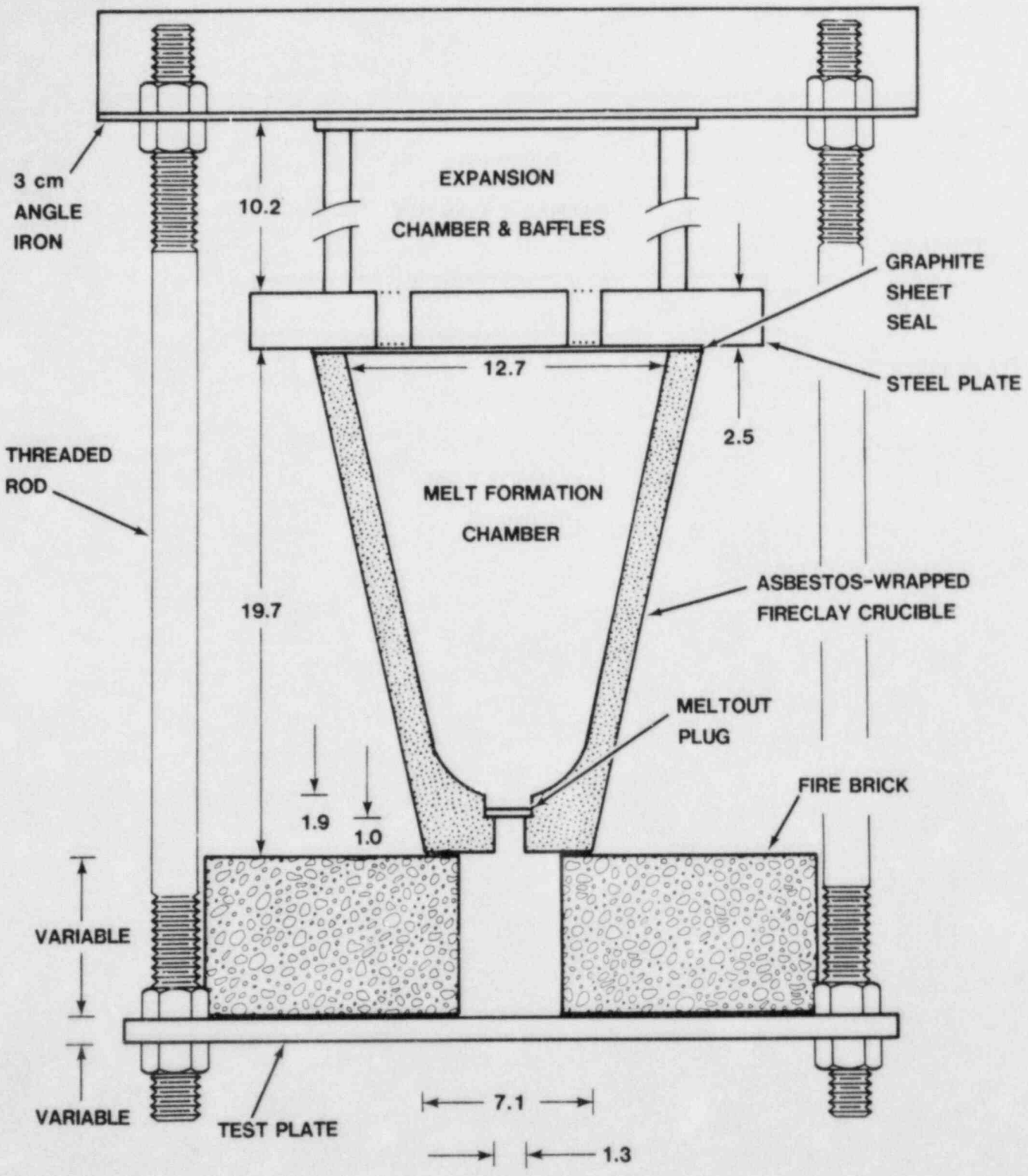

Figure 1. Cross-Sectional Side View of the Apparatus (Dimensions in cm).

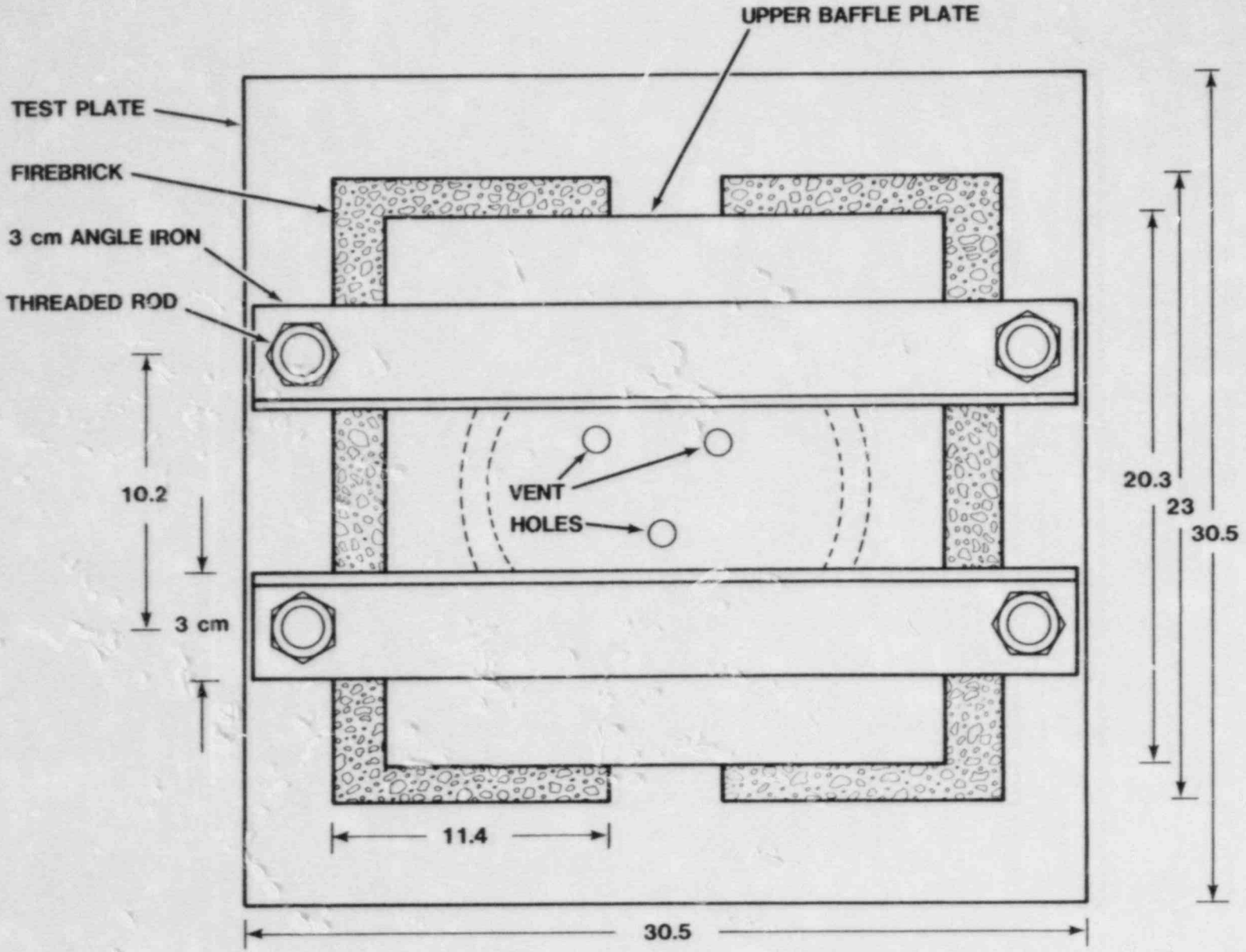

Figure 2. Top View of the Apparatus
(Dimensions in cm).

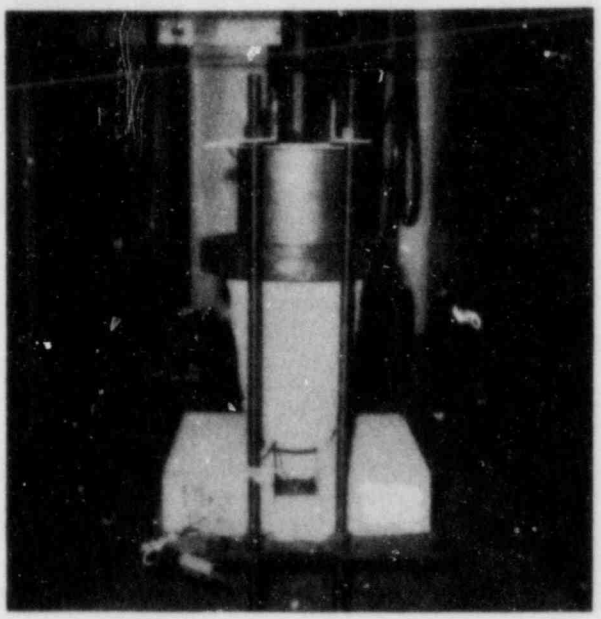

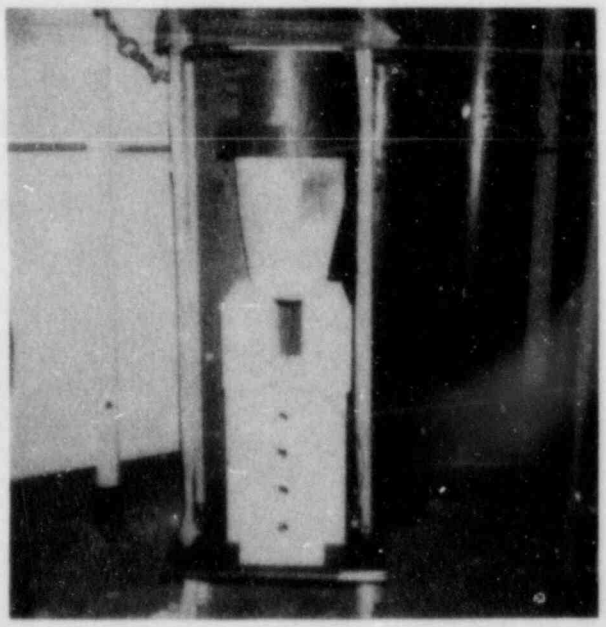

Figure 3. Photographs of the Apparatus Used in Tests PLATE #6 and PLATE #8.

allowed sufficient time for gases to vent from the reaction chamber prior to expulsion of the melt.

The one exception to the configuration described above was that used in test PLATE #7. In this test the hole in the base of the melt crucible was 5.1 cm in diameter. An aluminum disk 5.5 cm in diameter and 0.16 cm thick was used as the melt plug in this test.

The crucibles were supported above the target plates on parallel firebricks. The height of the crucible above the target plate could be adjusted between 6.4 and 34.3 cm by changing the orientation or number of supporting firebricks. Most of the tests were done with the crucible 11.4 cm above the target plate. The distance between the bottom of the melt plug and the surface of the target plate was then 12.1 cm.

The firebrick supports constrained the exposed region of the target plate to be a slot about 5 cm wide. The test apparatus was set so that melt would drain off after it had hit the plate.

Test PLATE #15 was an exception. In this test a quadrangle of firebricks was used to support the crucible and a pool of melt about 5 cm square was collected on the target plate.

Horizontal wires at about 2.5 cm intervals were placed between the support bricks. Melt could be seen passing these wires in photographic records of the tests. This permitted melt velocities to be determined from the photographic records.

The crucibles were capped by a 2.5 cm thick steel plate. The top of the crucible was ground flat and four 0.13 mm thick graphite sheets were placed on top of the crucible to insure the seal of the steel plate to the crucible. Three 1.3 cm diameter holes in the plate allowed gases to vent from the crucible. The hot gases that escaped from the crucible passed through a chamber filled with stainless turnings and then through a second steel plate 0.6 cm thick. This second plate was perforated with 0.6 cm diameter holes. The entire assembly was held in compression by angle irons bolted with four threaded rods attached to the target plate.

The mild steel and type 304 stainless steel test plates used in these experiments were 30.5 cm square. Plates 0.95 to 1.9 cm thick were used. Most tests were done with 0.95 cm

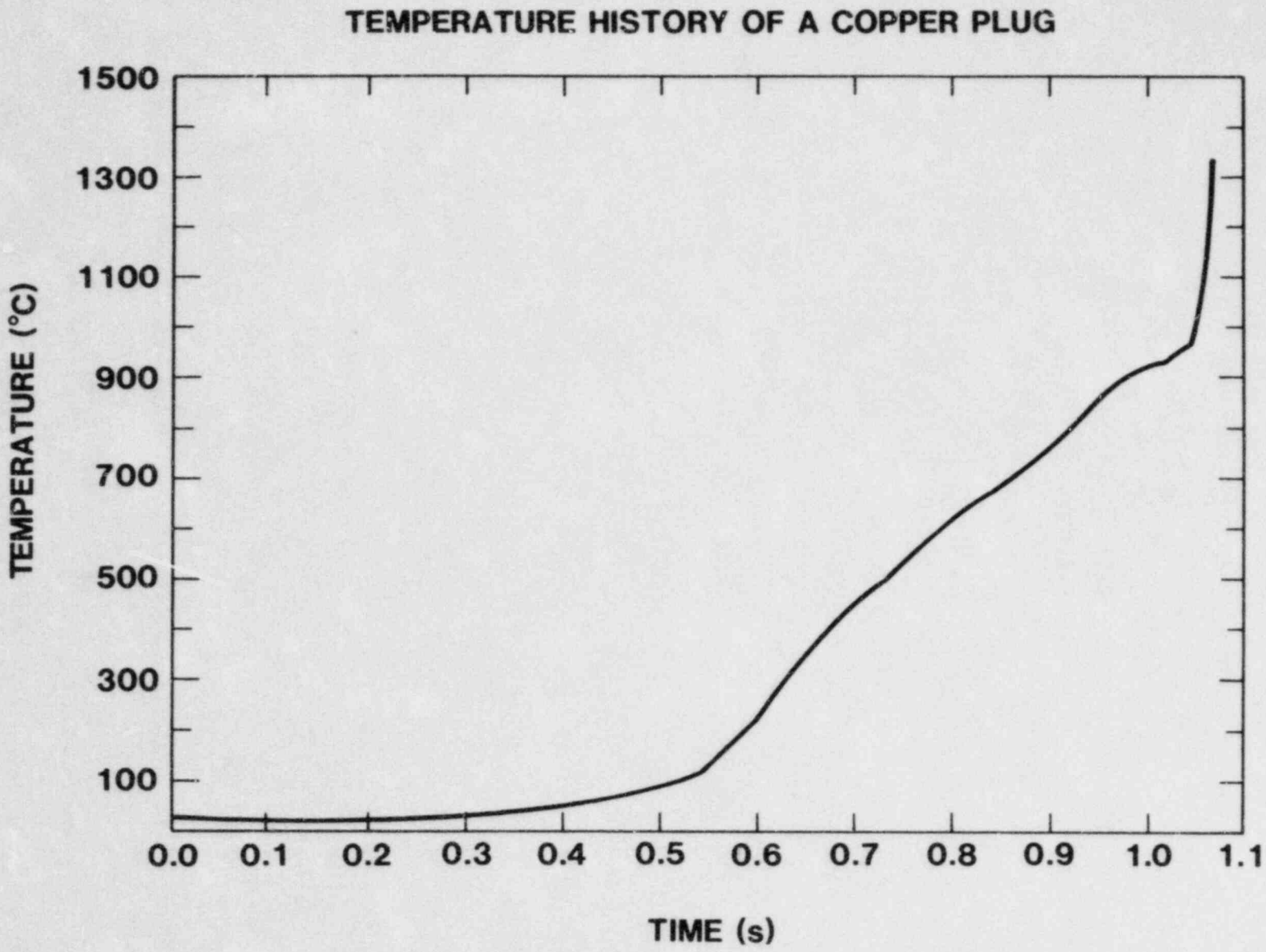

Figure 4. Temperature History of a Copper Melt Plug.

thick plates. All plates were tested in the as-received condition. Urania coatings were put on some plates by plasma spraying hyperstoichiometric urania ($UO_{2.06}$) in air. X-ray powder diffraction analysis of the coating was used to determine that the final coatings probably had the stoichiometry U_4O_9 (see Table I). After a test the stoichiometry of the urania was U_3O_8 (see Table I), but the coating still adhered to the plate. Coatings of urania 0.23, 1 and 2 mm thick were used in the tests. Two tests (tests PLATE #15 and PLATE #17) were done with mild steel plates coated with 2 mm of urania. In test Plate #17 the iron-alumina melt was forced to stream off of the plate after impact. This was the procedure used in tests with uncoated plates. In test Plate #15, fire clay bricks were configured to collect the melt in a pool on the coated plate. Photographs of the coating used in test PLATE #15 are shown in Figure 5.

A conventional thermite mixture (76.3 w/o Fe_3O_4; 23.7 w/o Al) was used to form the iron-alumina melts (55.2 w/o Fe; 44.8 w/o Al_2O_3). A detailed description and analysis of this reaction mixture has appeared elsewhere (2). This analysis indicates that the reaction mixture achieves temperatures in excess of 2530°C.

The reaction mixture used to form "corium" melts (54 w/o UO_2; 16 w/o ZrO_2; 30 w/o stainless steel) is shown in Table II. An analysis of the reaction is presented in Appendix A. This analysis indicates that reaction temperatures are as high as 2776°C. The limitation to the reaction temperature is produced by the boiling of the stainless steel phase.

The metallothermic reaction mixtures were ignited at the top with an electrically initiated fuze. Previous experiments (2) have shown that the conventional thermite mixture reacts smoothly and burns downward along a nearly planar front at a constant velocity. The corium mixture reacts more violently and rapidly than the conventional thermite.

Table I. X-Ray Powder Diffraction Data for Urania Coatings

Observed for Coating				Literature Data					
Pretest		Post-Test		UO_2		U_4O_9		U_3O_8	
d(A^o)	Intensity*	d(A^o)	Intensity*	d(A^o)	Intensity	d(A^o)	Intensity	d(A^o)	Intensity
3.133	S	4.1	S	3.157	100	3.14	100	5.85	4
2.714	M	3.4	M	2.735	48	2.72	45	4.1[illegible]	95
1.522	M	2.61	M	1.934	49	1.924	50	3.43	100
1.639	M	2.06	W	1.649	47	1.641	50	3.36	55
1.570	W	1.94	VW	1.579	13	1.571	16	2.642	75
1.358	VW	1.76	M	1.368	9	1.360	10	2.610	35
		1.42	W	1.255	18	1.248	30	2.073	20
				1.223	15	1.217	25	1.993	14
				1.116	13	1.111	20	1.952	20
				1.052	15	1.047	25	1.796	16
								1.774	50
								1.714	14
								1.421	18

*S = strong; M = medium; W = weak; VW = very weak

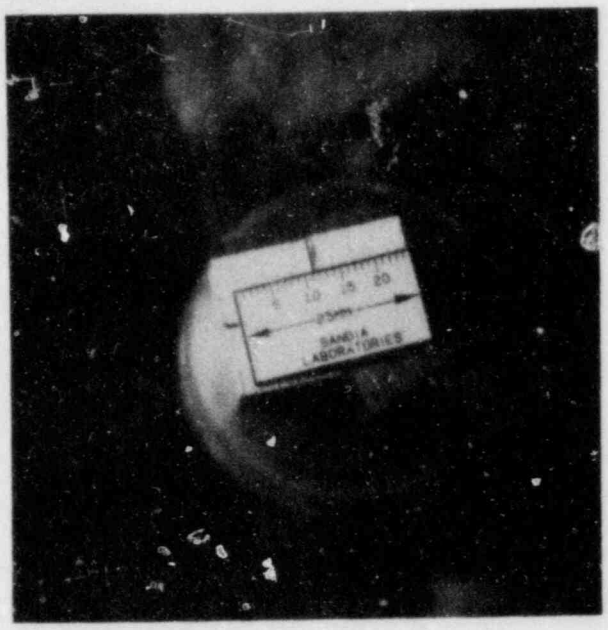

(a) Macrophotograph of Plasma-Sprayed Urania Coating on the Steel Plate used in Test PLATE #15.

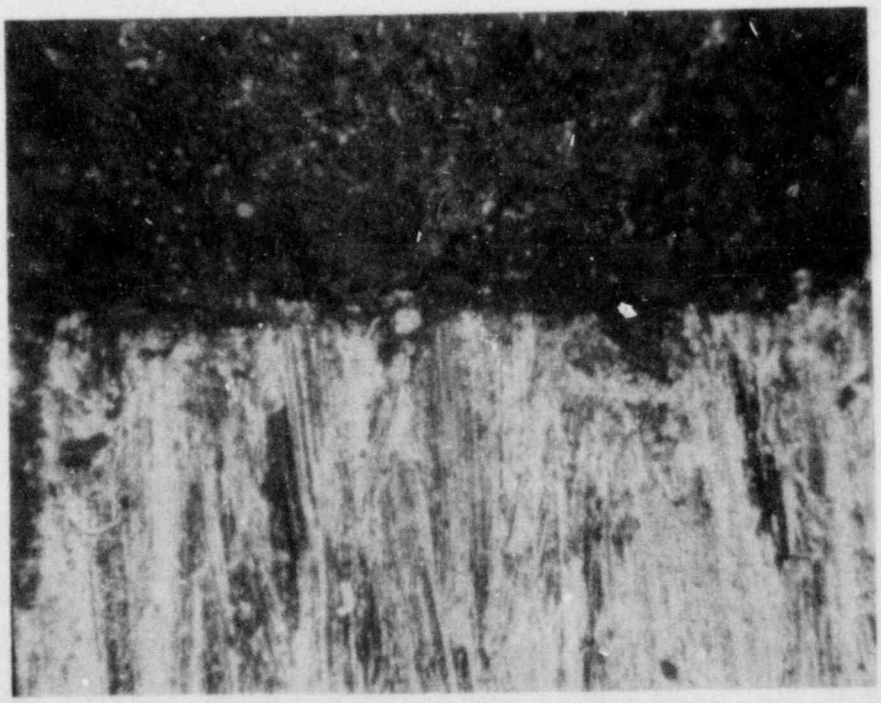

(b) 50x Magnification of the Coating/Steel Interface.

Figure 5. Photographs of the Urania Coating Used in Test Plate #15.

Table II. Constituents of the Corium Reaction Mixture

Constituent	Amount (w/o)	Supplier
Zirconium Powder	11.9	AMAX
Uranium Powder	47.5	Y-12
Chromium Trioxide	7.8	Ventron
Nickel Oxide	2.3	Ventron
Magnetite	23.0	Chemalloy
Stainless Steel	7.5	Ventron

Evidence from test PLATE #16 suggests this mixture did not react along a planar front and the reaction may not have been complete at the time the melt plug at the bottom of the crucible fused.

Instrumentation of the tests consisted of thermocouples and motion picture records of the tests. Thermocouples were located at the ignition point of the fuse for the charge, the ignition point of the charge, the bottom surface of the copper plug, the top of the structure being exposed to melt and the bottom surface of the structure. Thermocouples at all locations except the bottom surfaces of the structures being exposed to melt were used primarily for timing purposes. These were bare junction, type K thermocouples fabricated from 0.05 cm wires and insulated with an asbestos cloth. Thermocouples on the top surface of exposed structures were not attached to these structures.

Thermocouples on the copper slugs in the crucible and the bottoms of the structures exposed to melt were spot welded in place. These sensors were of the "separated junction" design. A typical configuration of thermocouples on the bottom of a structure is shown in Figure 6. Both type K and type S thermocouples were used in these locations. The type K thermocouples were similar to those used elsewhere. Type S thermocouples, also fabricated with 0.05 cm wires, were insulated with alumina beads.

Thermocouple outputs were recorded on a Honeywell model 5800 Visicorder. The chart speed was 50.8 cm/sec. This allowed time resolution of the data to $\pm$0.001 seconds. Outputs from the thermocouples could be resolved to $\pm$0.2 mv and $\pm$0.1 mv for type K and type S thermocouples, respectively. For the type K thermocouples this amounts to a temperature resolution of $\pm 5^{o}C$. For type S thermocouples the resolution is about $\pm 16^{o}C$.

Photographic records of the tests were made at 24 and 400 frames per second. These recording rates allowed time resolution of test events to $\pm$0.04 and $\pm$0.0025 seconds, respectively.

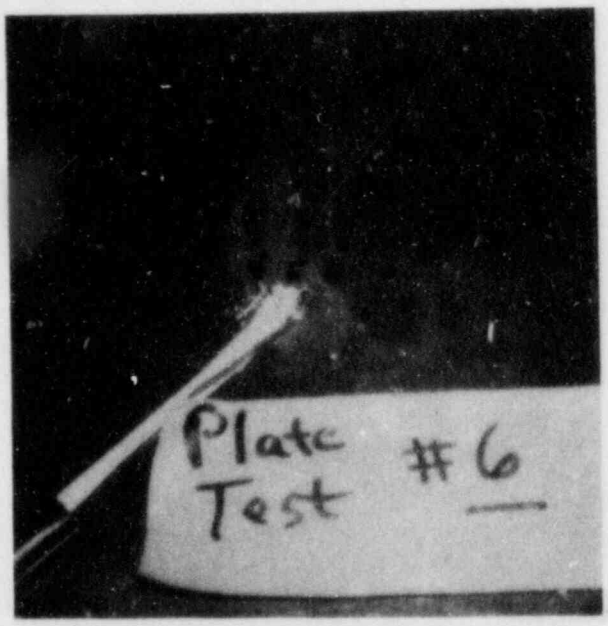

Figure 6. Example of Thermocouples Attached to the Bottom of a Steel Plate to be Exposed to Melt.

III. RESULTS

A) EVENTS OF THE TESTS

A summary of the twelve tests run in the PLATE series is shown in Table III. A photograph of a typical test (PLATE #11) is shown in Figure 7. Most of the tests behaved in the expected manner. The melt-forming reaction mixture was ignited, once the reaction was complete, venting from the reaction crucible ceased, the melt plug at the base of the crucible was penetrated, and melt streamed onto the target plate and eventually penetrated the plate.

Tests PLATE #7 and PLATE #16 were exceptions to this behavior. In test PLATE #7 a large diameter melt plug was used. This plug did not fail catastrophically. Rather, it melted on one side first. The emerging stream of melt bounced off the firebrick containment and sprayed in a fan shape over the surface of the test plate. Failure of the melt plug occurred before the venting of the reaction crucible was complete. The emerging melt stream appeared to have a higher velocity than that in an analogous test with a small drain oriface. No measurements of the stream velocity were possible because the stream bounced off the firebrick.

In test PLATE #16 which used a corium melt, the melt plug failed prior to complete venting and the melt stream velocity was demonstrably higher than in analogous tests in which venting was complete.

Tests PLATE #15 and PLATE #17 were also exceptions to the general test behavior. In both these tests the target plate was coated with 2 mm of urania. In neither test did the melt stream penetrate the target plate.

A summary of the timing data from the tests is presented in Table IV. In general, the chemical reaction to form the melt required about 11 seconds. The corium melt-forming reaction was significantly faster. This reaction was nearly complete in about 5 seconds. Melts usually streamed from the reaction crucibles for about 5 seconds. The overall mass flow rates were then about 600 grams per second. Again test PLATE #16 was exceptional. The corium melt was expelled in about 3.4 seconds so the overall mass flow rate was about 1460 grams per second. The lower expulsion time in test PLATE #16 probably arose because the crucible was still pressurized when melt began to stream onto the target plate. The higher mass flow rate in test PLATE #16 was due to both the higher density of the melt material and the more rapid expulsion rate.

Table III. Summary of the Experiments

Test	Melt Mass and Composition[a]	Plate Thickness[b] (cm)	Oxide Coat Thickness (mm)	Orifice Size (cm)	Drop Height (cm)
PLATE #5	2500g Fe + Al_2O_3	0.953	0	1.27	12.4
PLATE #6	3000g Fe + Al_2O_3	0.953	0	1.27	7.4
PLATE #7	2886g Fe + Al_2O_3	0.953	0	5.1	10.8
PLATE #8	3000g Fe + Al_2O_3	0.953	0	1.27	35.3
PLATE #10	3000g Fe + Al_2O_3	1.27	0	1.27	12.4
PLATE #11	3000g Fe + Al_2O_3	1.90	0	1.27	12.4
PLATE #12	3000g Fe + Al_2O_3	0.953	0.23	1.27	12.4
PLATE #14	3000g Fe + Al_2O_3	0.953	1.0	1.27	12.4
PLATE #15	3000g Fe + Al_2O_3	0.953	2.0	1.27	12.4
PLATE #16	5000g Corium	0.953	0	1.27	12.4
PLATE #17	3000g Fe + Al_2O_3	0.953	2.0	1.27	12.4
PLATE #20	3000g Fe + Al_2O_3	1.27 SS	0	1.27	12.4

(a) Fe + Al_2O_3 = 55 w/o Fe and 45 w/o Al_2O_3; Corium = 54 w/o UO_2; 16 w/o ZrO_2 and 30 w/o stainless steel.

(b) Plate material was mild steel except for test PLATE #20 in which type 304 stainless steel was used.

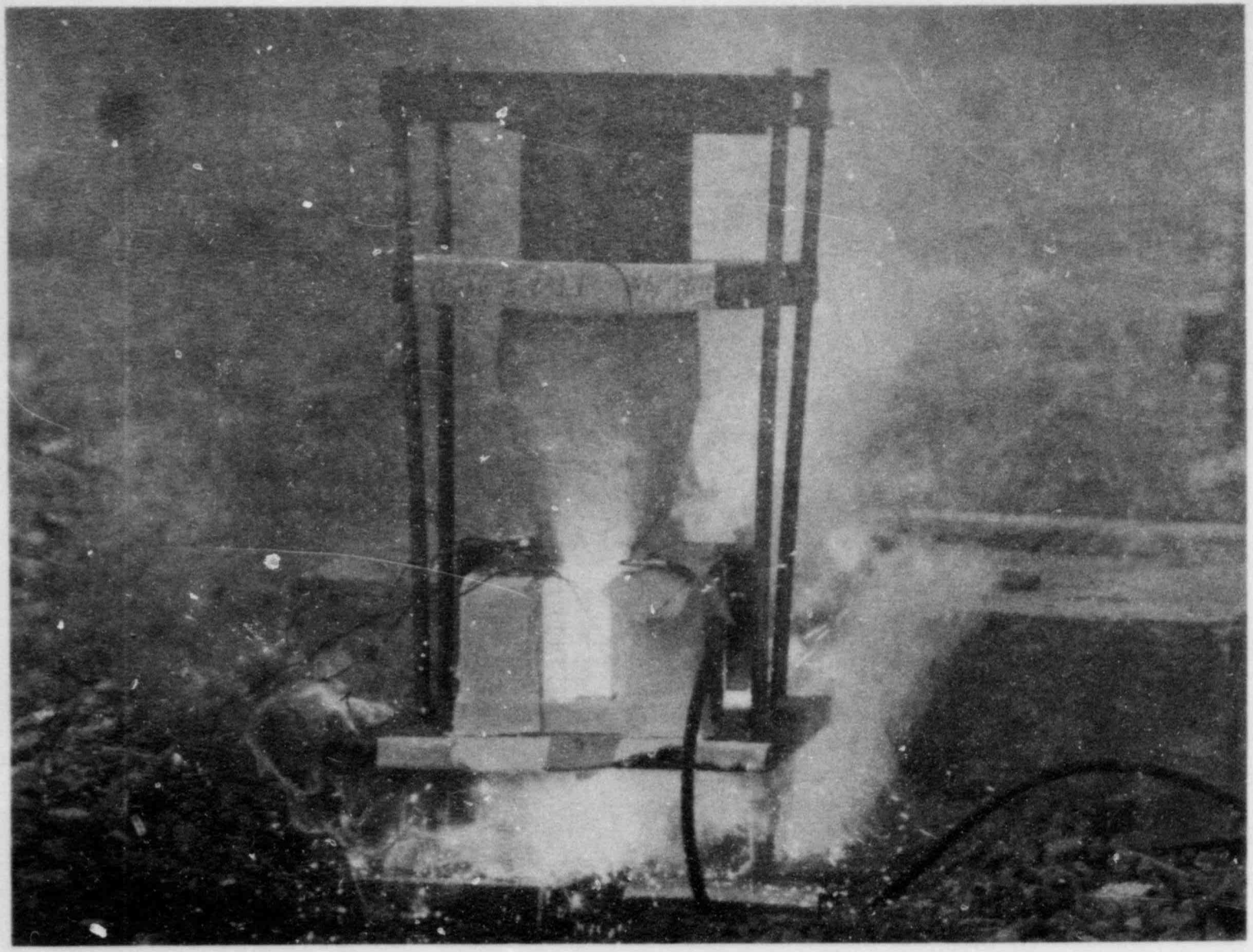

Figure 7. Test PLATE #11 Just After Melt Penetrated the 1.9 cm Steel Plate.

Temperature data obtained in the tests are collected in Appendix B. These data show that high temperatures are reached at the backside of the plates only fractions of a second prior to penetration. The cool, strong layer at the back of the plates means that mechanical processes such as creep rupture contribute little to the penetration of the plates in these tests. This is consistent with previous analyses of the penetration problem (1).

B) IMPACT VELOCITIES OF THE MELTS

Inspection of photographic records of the tests allowed measurement of the stream velocities during their passage from the crucible to the plate. Data typically could be obtained only for the first part of the melt to emerge from the crucible. Aerosols obscured the melt jets later in the tests and the jets were featureless so there were no reference points to track even when aerosol clouds momentarily dissipated.

Data collected from the photographic records consisted of the time, t_i, the melt front passed a location that was a distance, d_i, from the bottom of the melt-out plug. Results for all the tests except tests PLATE #7 and PLATE #16 were consistent. These data are plotted as velocity $[(d_1 - d_2)/(t_1 - t_2)]$ against distance of travel $[(d_1 + d_2)/2]$ in Figure 8. It was found that the data could be correlated assuming simple acceleration without considering drag. The correlation was improved if it was assumed the 1.0 cm nozzle below the melt plug exerted sufficient drag on the melt that when the melt emerged from the crucible, it had essentially zero velocity. This improved correlation is shown as a solid line in Figure 8.

Since no measurements of melt velocity at the exact point of impact could be made, this velocity was inferred from the correlation line in Figure 8 and the distance between the melt plug and the test plate. These inferred impact velocities are listed in Table IV. It is assumed throughout the discussion below that melt velocities at impact were constant during the tests and were equal to the initial impact velocity.

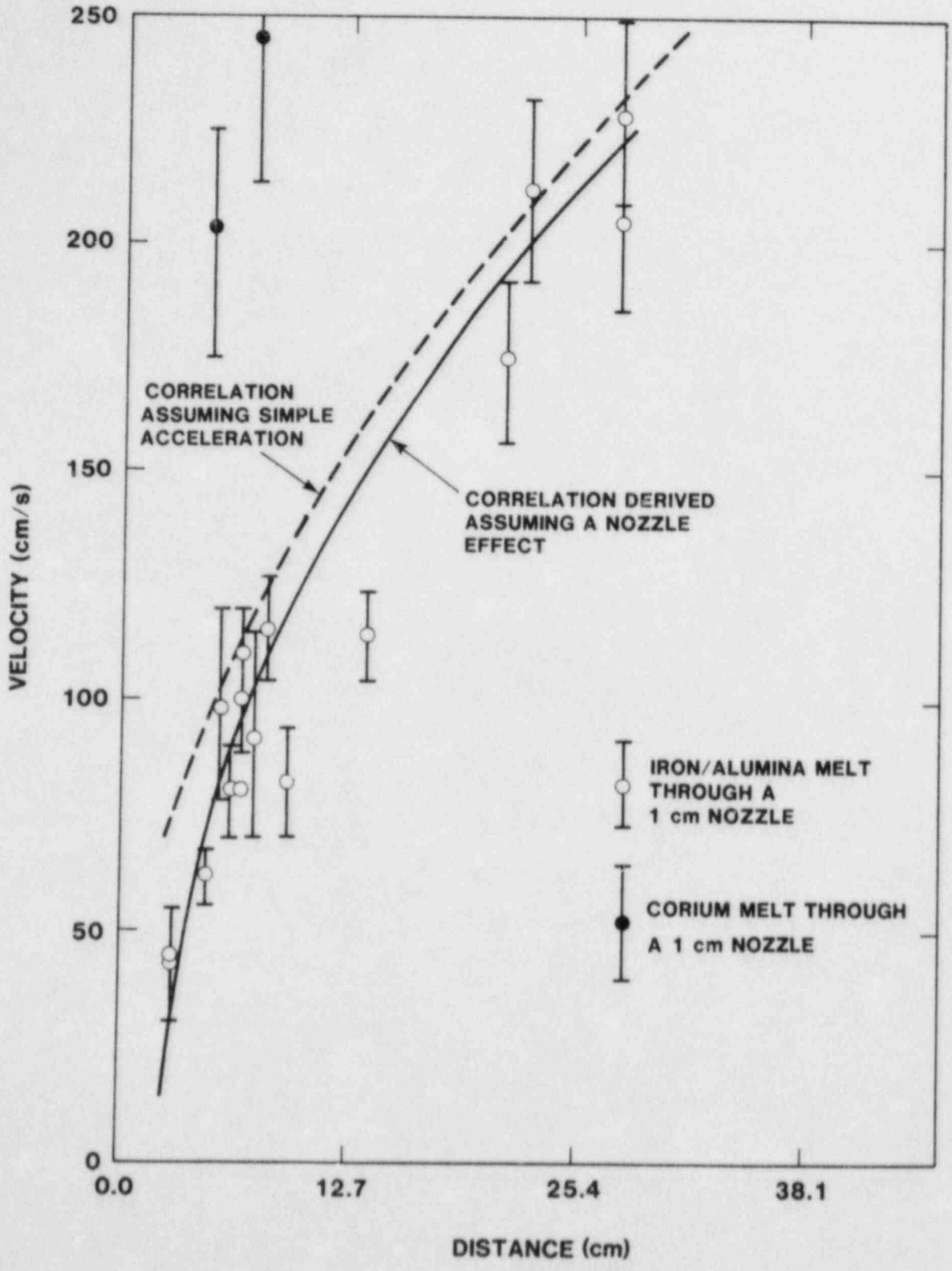

Figure 8. Melt Velocity as a Function of the Distance from the Melt Plug.

Table IV. Summary of Data from the Tests

Test	Reaction Time (s)	Deposition Time (s)	Penetration Time (s)	Hole Size (cm)	Impact Velocity (cm/s)
PLATE #5	11.98	5.38	0.98	2.5 - 2.9	143
PLATE #6	nd**	5.075	1.087	2.2	102
PLATE #7	nd**	5.422	0.62	5.1 x 2.2*	nd**
PLATE #8	10.85	4.72	0.759	3.5	255
PLATE #10	12.25	5.033	1.292	2.5	143
PLATE #11	12.0	5.083	1.933	1.9	143
PLATE #12	8.98	4.938	1.338	2.5	143
PLATE #14	nd**	5.29	2.290	1.9	143
PLATE #15	11.82	5.23	did not penetrate		143
PLATE #16	4.88	3.38	2.20	2.5	270
PLATE #17	12.85	5.44	did not penetrate		143
PLATE #20	14.84	5.154	1.192	2.5	143

* ellipsoidal
** not determined

Only two velocity measurements were obtained from the photographic record of test PLATE #16. These measurements are shown in Figure 8. To estimate the impact velocity of the corium melt it was assumed that this stream was also accelerated by gravity but that it had a non-zero initial velocity when it emerged from the crucible.

C) PERFORATION OF PLATES

Photographs of the perforations produced in the plates by the melts are presented in Figures 9-12. With the exception of the hole in the plate from test PLATE #7, the holes are essentially circular. The hole in the plate from test PLATE #7 is ellipsoidal as would befit the fan-shaped stream that developed in this test.

The holes in the plates as well as images of the melt streams in photographic records of the tests indicate that the streams remained fairly compact in flight. The holes are roughly twice the diameter of the drain orifice in the reaction crucible. The holes are largest for streams that fell the greatest distances and consequently had the highest velocities.

The hole in a plate represents to a first approximation the region over which heat flux from the melt to the plate was relatively uniform. Spread in this region relative to the cross-sectional area of the steam is to be expected for stagnation flow. Experimental studies of stagnated jets indicate the spread region should be about 1.75 times the jet diameter (3) and varies approximately linearly with jet velocity (4).

Since the jets in the PLATE tests are accelerated under the influence of gravity, the stream diameter at impact narrows as the drop distance increases. Simple geometric arguments based on the narrowing of the stream during its fall and the increase in the spread of the high heat flux region with velocity lead to the conclusion that

$$H_i \propto \sqrt{V_i}$$

where

H_i = diameter of the i^{th} hole

V_i = velocity of the i^{th} jet at impact

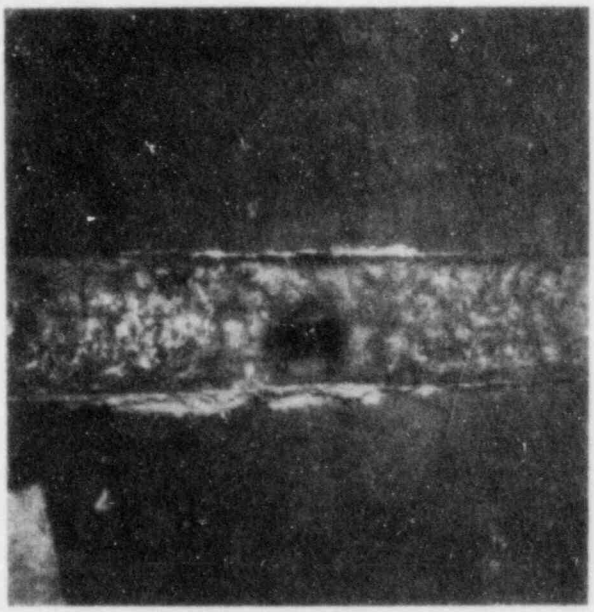

(a) Top View of the Penetration in Test PLATE #5.

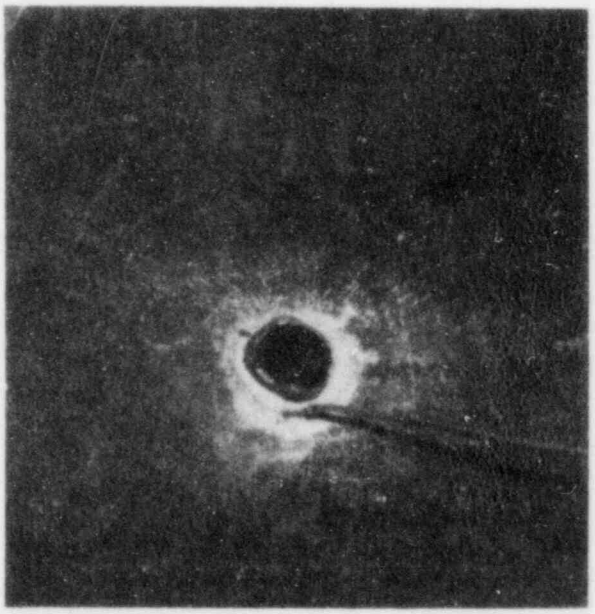

(b) Bottom View of the Penetration in Test PLATE #5.

(c) Bottom View of the Penetration in Test PLATE #6.

Figure 9. Penetrations Produced in Tests PLATE #5 and PLATE #6.

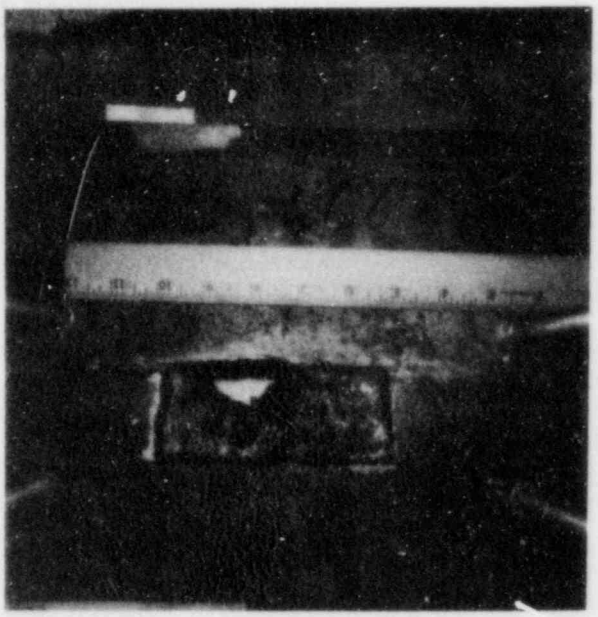

(a) Top View of the Penetration in Test PLATE #7.

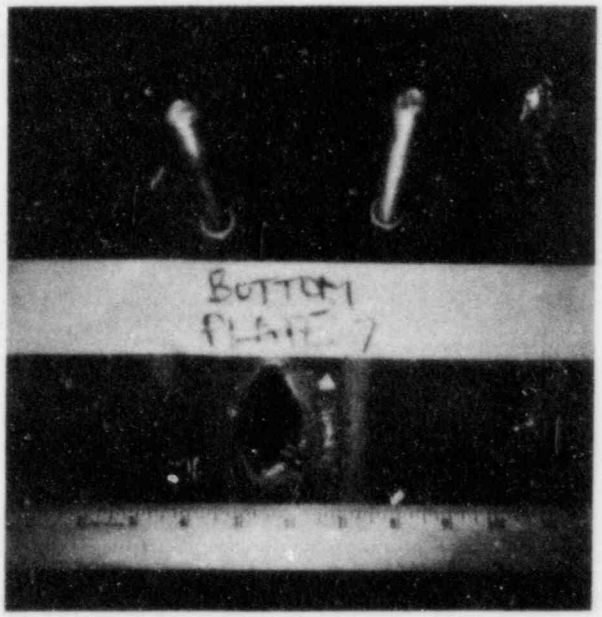

(b) Bottom View of the Penetration in Test PLATE #7.

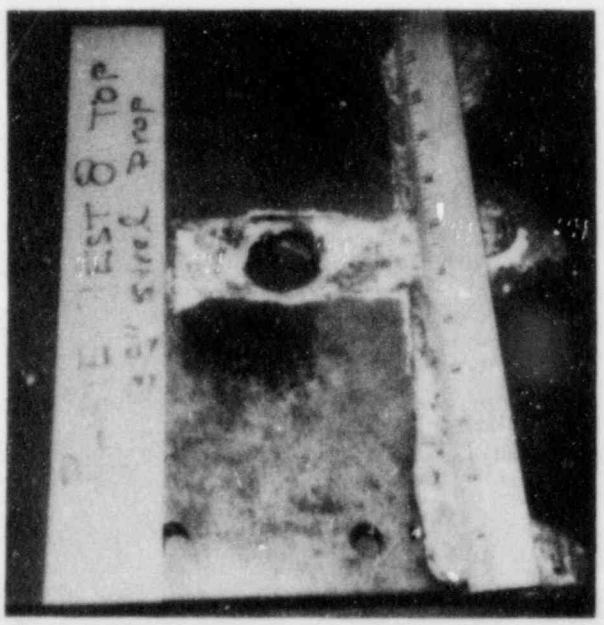

(c) Bottom View of the Penetration in Test PLATE #8.

Figure 10. Penetrations Produced in Tests PLATE #7 and PLATE #8.

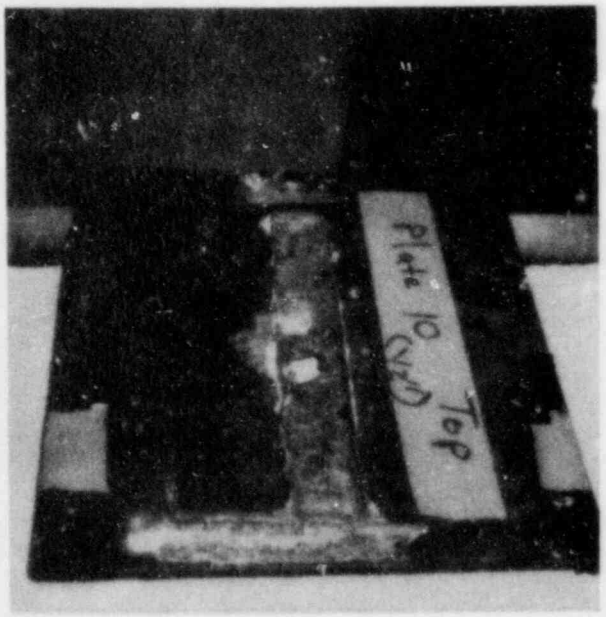

(a) Top View of the Penetration in Test PLATE #10.

(b) Bottom View of the Penetration in Test PLATE #10.

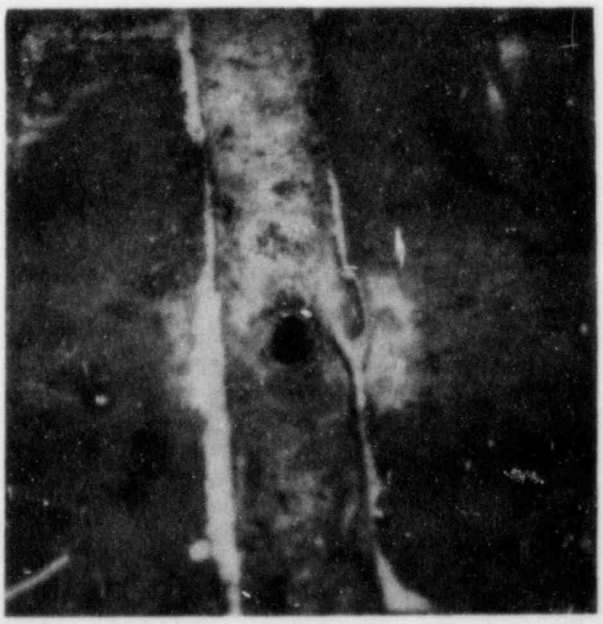

(c) Top View of the Penetration in Test PLATE #11.

(d) Bottom View of the Penetration in Test PLATE #11.

Figure 11. Penetrations Produced in Tests PLATE #10 and PLATE #11.

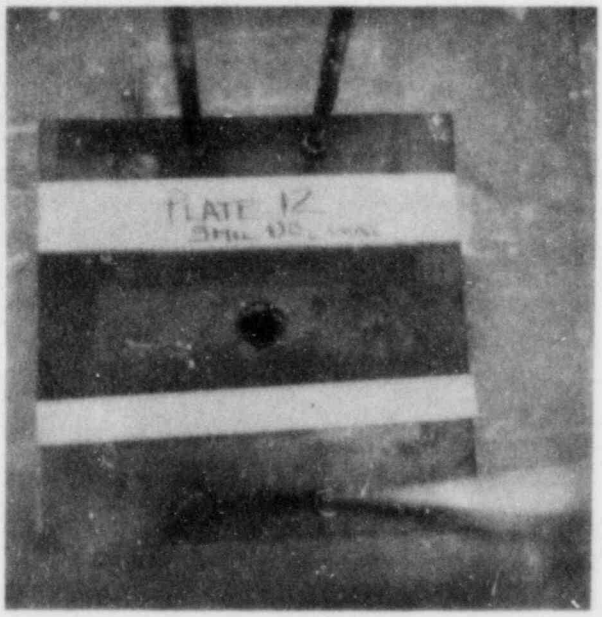

(a) Top View of the Penetration in Test PLATE #12.

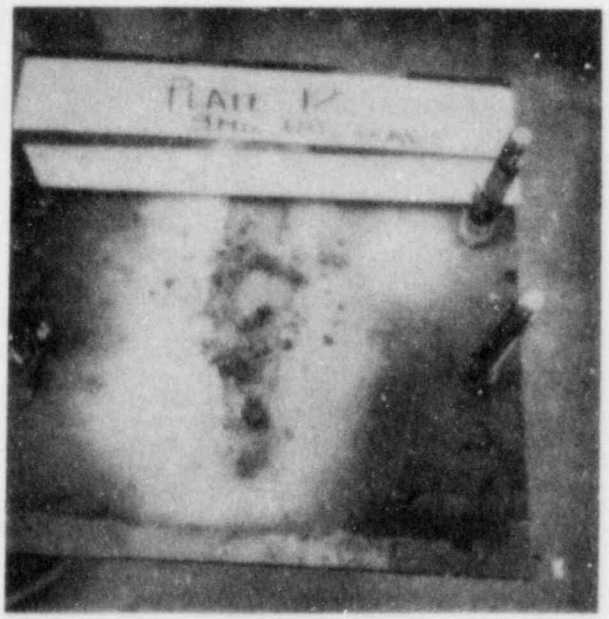

(b) Bottom View of the Penetration in Test PLATE #12.

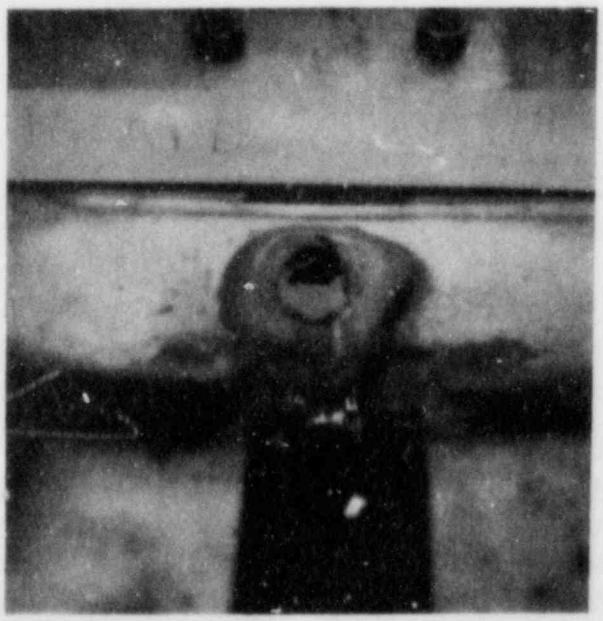

(c) Bottom View of the Penetration in Test PLATE #20.

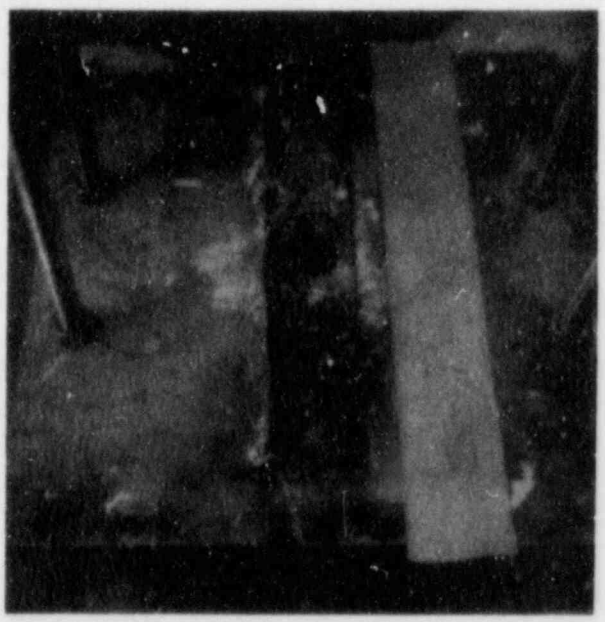

(d) Top View of the Penetration in Test PLATE #20.

Figure 12. Penetration Produced in Test PLATES #12 and PLATE #20.

Data from the PLATE tests cover too narrow a velocity range to test the proportionality between holes size and the square root of velocity. As shown in Figure 13 the results are consistent with the proportionality. Considering the tests to be experiments with stagnated, high temperature, melt jets seems reasonable.

D) EMPIRICAL CORRELATION OF THE TEST RESULTS

The tests in the PLATE test program may be grouped into four series of tests to explore three variables systematically and point tests of melt compositon and plate composition:

(1) Plate Thickness: tests to examine the time for a melt jet to penetrate a steel plate as a function of plate thickness (tests PLATE #5, PLATE #10 and PLATE #11).

(2) Melt Velocity: tests to examine the time for a melt jet to penetrate a steel plate as a function of jet velocity (tests PLATE #5, PLATE #6 and PLATE #8).

(3) Urania Coatings: tests to examine the time required for melt jets to penetrate steel plates coated with various thicknesses of urania. (Tests PLATE #5, PLATE #12, PLATE #14, PLATE #15 and PLATE #17)

(4) Point Tests: (a) the effect of melt composition on the rate of penetration is found by comparing the results of tests PLATE #16 and PLATE #5; (b) the effect of jet diameter was to be shown by comparing the results of tests PLATE #7 and PLATE #5; (c) the effects of steel thermal properties are shown by comparing the results of test PLATE #20 and PLATE #10.

Strictly empirical correlations of the test results are presented below.

Penetration times for tests in which the thickness of the target plate was the variable are shown in Figure 14. Linear correlation of the penetration time with distance yields:

$$t = (1.002 \pm 0.0066)\, d(cm) + (0.02336 \pm 0.0095)$$

where

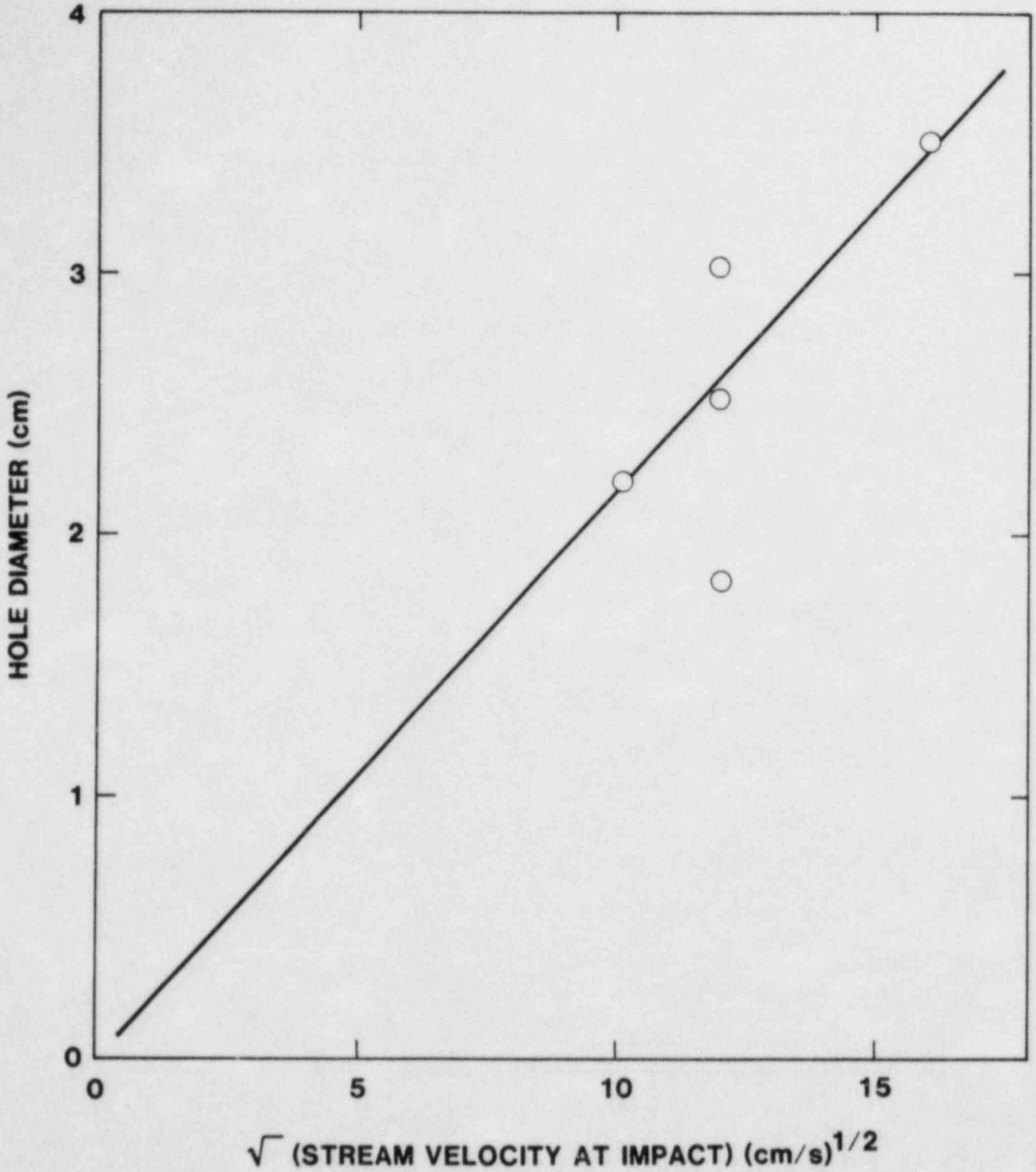

Figure 13. Plot of Penetration Diameter Against the Square Root of the Melt Velocity at Impact.

d = plate thickness
t = time (s) to penetration.*

The correlation coefficient for the regression is 0.99998. The probability of a random data set of 3 points yielding such a high correlation coefficient is less than 5%. The finite intercept is distinguishable from zero to a confidence level of about 80%. This finite, positive, intercept may be indicative of some crust formation when melt first contacts the steel target as has been observed in previous tests (1). The thermal criterion for crust formation is that the interface temperature, T_i, found from

$$\left[\frac{T_i - T_m}{T_s - T_i}\right]^2 = \frac{C_s \rho_s K_s}{C_m \rho_m K_m}$$

where

C = heat capacity

K = thermal conductivity

ρ = density

m = subscript indicative of melt

s = subscript indicative of the steel plate

T_m = bulk melt temperature

T_s = initial steel temperature

be less than the freezing point of the melt. If the melt is taken to be iron, the condition for crust formation is just met. Were the melt stainless steel, a frozen crust would not be expected.

Attempts to analyze the tests with finite difference heat conduction model described elsewhere (1) revealed no significant crust formation. At most, a crust less than 0.02 cm thick that lasts for 0.002 seconds could be predicted.

---

* Errors associated with parametric values in this and other correlation expressions presented here are $\pm$ one standard deviation.

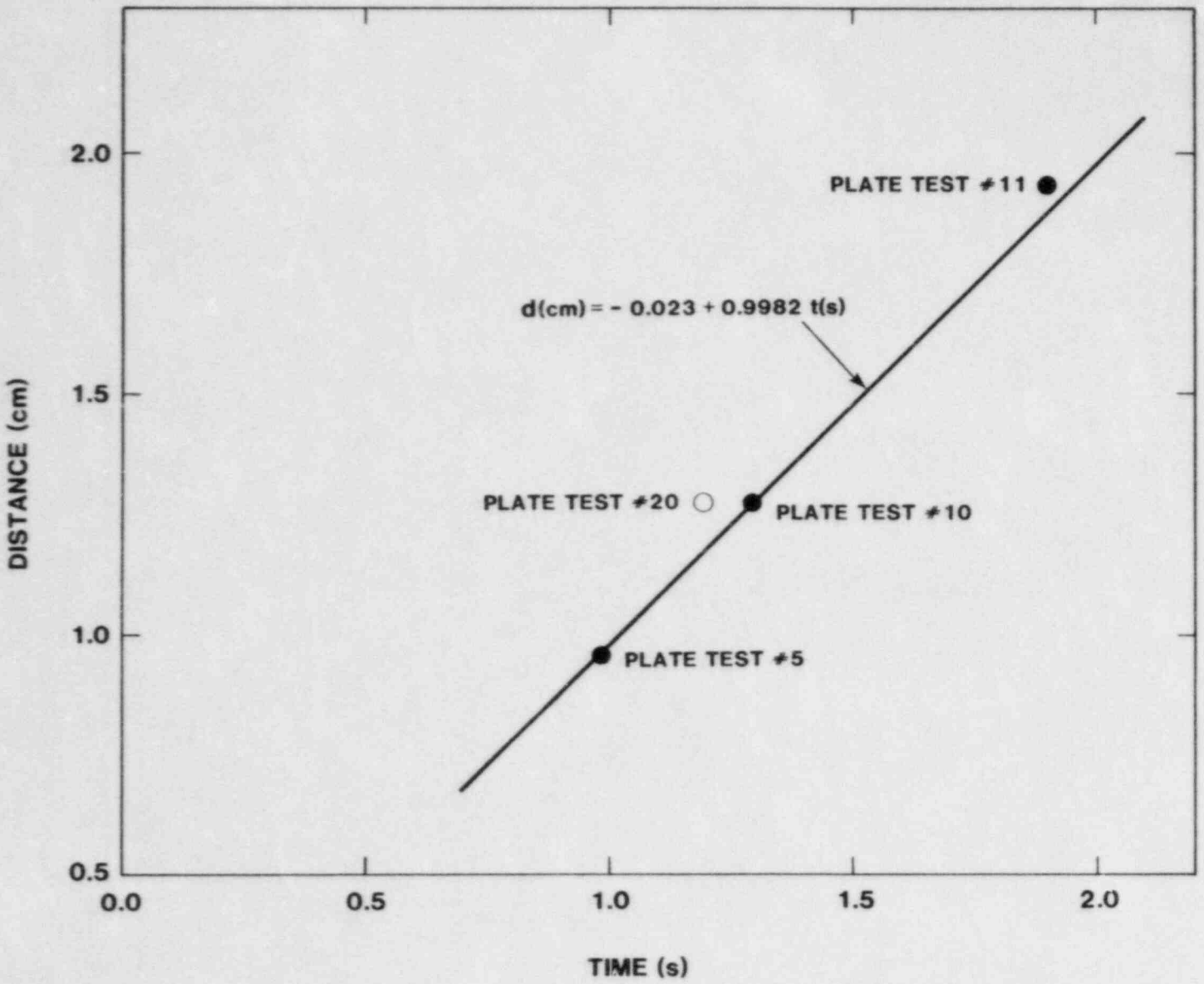

Figure 14. Time Required for Melt to Penetrate Plates of Various Thicknesses.

If penetration is considered to be the result of heating metal just beyond its melting point, the slope of the correlation indicates that heat fluxes being imparted to the melt amount to at least 2400 cal/cm^2-s.

Results for test PLATE #20 are also shown in Figure 14, but were not included in the derivation of the regression formula. Results from this test indicate somewhat faster erosion of stainless steel than mild steel. About 10% less energy is required to ablate stainless steel than mild steel. This lower energy requirement for ablation would account for the deviation of the result of test PLATE #20 from the regression line.

Penetration times are plotted in Figure 15 against the distance between the bottom of the melt plug and the target plate. An empirical correlation expression was developed for these data in terms of the melt velocity at impact:

$$\ln (t - 0.0234) = (-0.3973 \pm 0.0355) \ln(V) + (1.9327 \pm 0.1795)$$

where

V = impact velocity (cm/s).

Correlation of t - 0.0234 rather than t was attempted in order to remove the effect of crust formation suggested by the correlation of penetration time with plate thickness. The regression correlation coefficient is -0.99603. Only about 10% of the time would a random data set yield such a high correlation coefficient. Had the time not been corrected for the possible effect of crust formation the correlation would be virtually the same:

$$\ln(t) = (-0.3574 \pm 0.0355)\ln(V) + (1.9331 \pm 0.17953)$$

The coefficient of the ln(V) term in the regression expression, -0.3973 $\pm$ 0.0355, is less than -0.5 to a confidence level of about 90%. Stagnation heat flux correlations typically predict penetration time will depend on velocity according to:

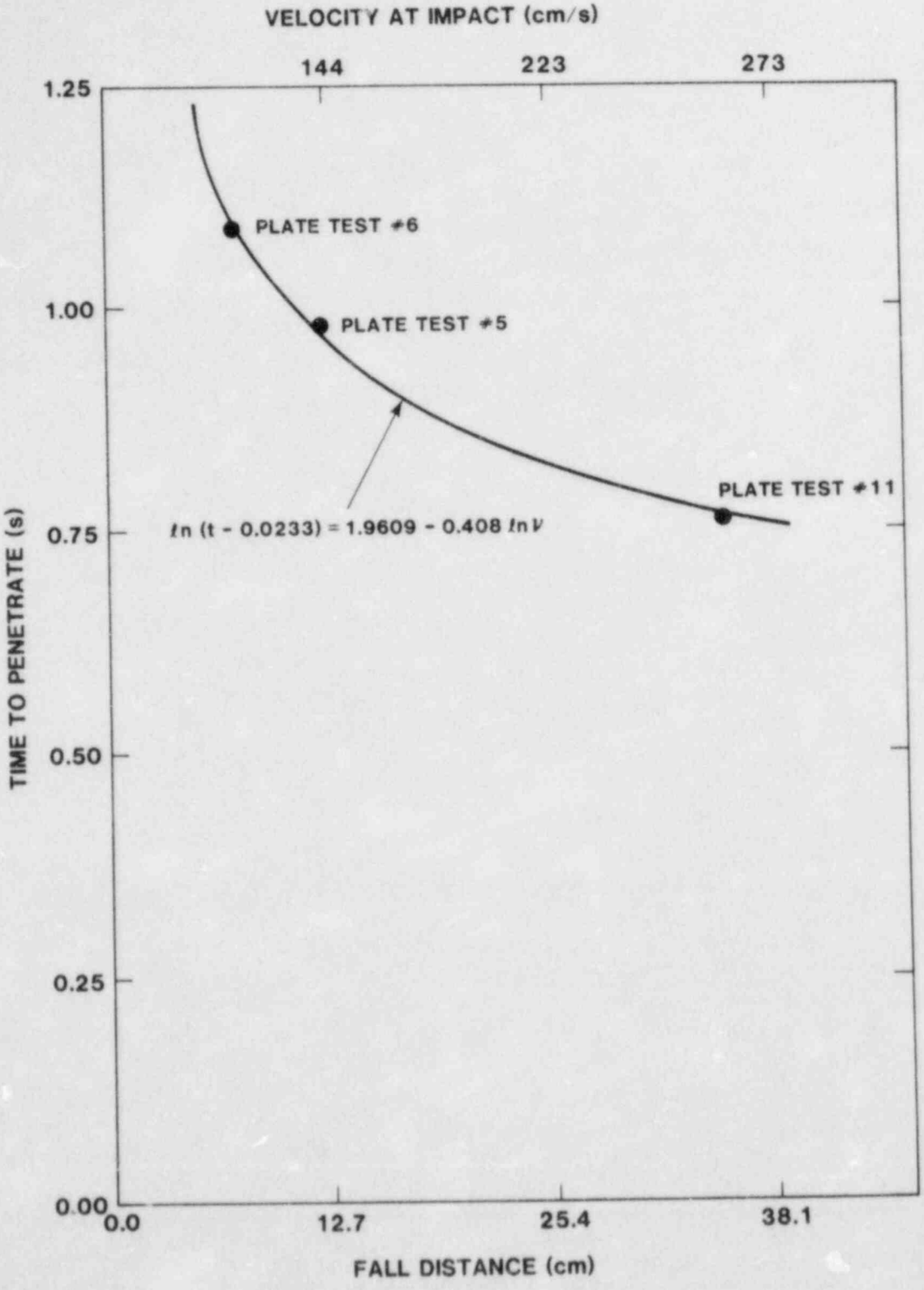

Figure 15. Penetration of Plates by Melts of Various Velocities.

$$t \propto \alpha \frac{1}{\sqrt{V}}$$

if the jet diameter is held constant (5). But in accelerated jets, the jet diameter decreases as the square root of velocity. Consequently,

$$t \propto \alpha V^{-3/4}$$

Clearly neither of these proportionalities between penetration time and a power of velocity agree with results of the PLATE tests. If, instead of the geometric jet diameter, the "spread" diameter discussed above in connection with holes in the plates is used in the stagnation heat flux correlations then

$$t \propto V^{-1/4}$$

which is also at odds with the empirical result obtained here. The empirical result requires that the effective diameter of the jet to be used in the stagnation heat flux correlation vary with the one fourth power of the velocity. Data from the PLATE tests are too sparse to determine if this relationship is obeyed. The available data are not inconsistent with this variation. Had test PLATE #7 been more consistent with other tests some more definitive indication of the role jet diameter plays in penetration might have been obtained.

Application of the correlation of penetration time with velocity to test PLATE #16 yields a predicted penetration time of 0.747 seconds. This is only about a third the observed penetration time. Clearly, melt composition may have a bearing on penetration time in the tests with corium melts. More extensive crust formation would be expected, based on thermal criteria, for jets of corium which have a higher refractory oxide content than mild steel jets. The delay in onset of ablation caused by formation and removal of a crust could explain the longer penetration time found in test PLATE #16.

E) EFFECTS OF URANIA COATINGS

Penetration of the steel plates was delayed by the presence of urania coatings on the plates. In test PLATE #12 in which the urania coating was 0.23 mm thick penetration occurred 0.358 seconds later than in the analogous test with an uncoated plate (test PLATE #5). When the coating was 1 mm thick (test PLATE #14) penetration was delayed 1.31 seconds. In both tests PLATE #12 and PLATE #14 there was no evidence that the coating failed by mechanical means. The coatings were found after the tests to be still firmly attached to the steel plates in the vicinity of the penetrations.

When the coatings were 2 mm thick (tests PLATE #15 and PLATE #17) no penetration occurred. In test PLATE #15 a pool of melt was collected on the target plate. This melt was welded to the coating. In test PLATE #17 melt was drained away after it had hit the target plate. The coating was largely undamaged at the location of melt impact in test PLATE #17.

The coating of urania is both more refractory and has a lower thermal conductivity than steel. To a first approximation the coating makes the plate "effectively" thicker. The reciprocal of the differences between the times of penetration of the coated and an uncoated plate are plotted against coating thicknesses in Figure 16. Results for tests PLATE #15 and PLATE #17 are plotted as though an infinite time would be required for penetration to occur. This is probably untrue. Had melt continued to pour onto the plates with 2 mm urania coatings these plates would also have been penetrated. Results shown in Figure 16 suggest the effect of the coating on penetration time is not linear. It might be expected on intuitive grounds to vary as the square of the coating thickness. There are insufficient data to develop a meaningful empirical description of the effects of urania coatings. It is clear, however, that such coating can have an important effect even when they are quite thin.

The urania coatings on the steel plates apparently reduce the heat flux to the underlying steel sharply. Temperature data from tests PLATE #15 and PLATE #17 (see Figures B-9 and B-11) were subjected to inverse heat flux analysis as described in Appendix C to determine the time dependent heat flux transmitted to the steel through the 2 mm oxide coating. Results of these analayses are shown in Figures 17 and 18.

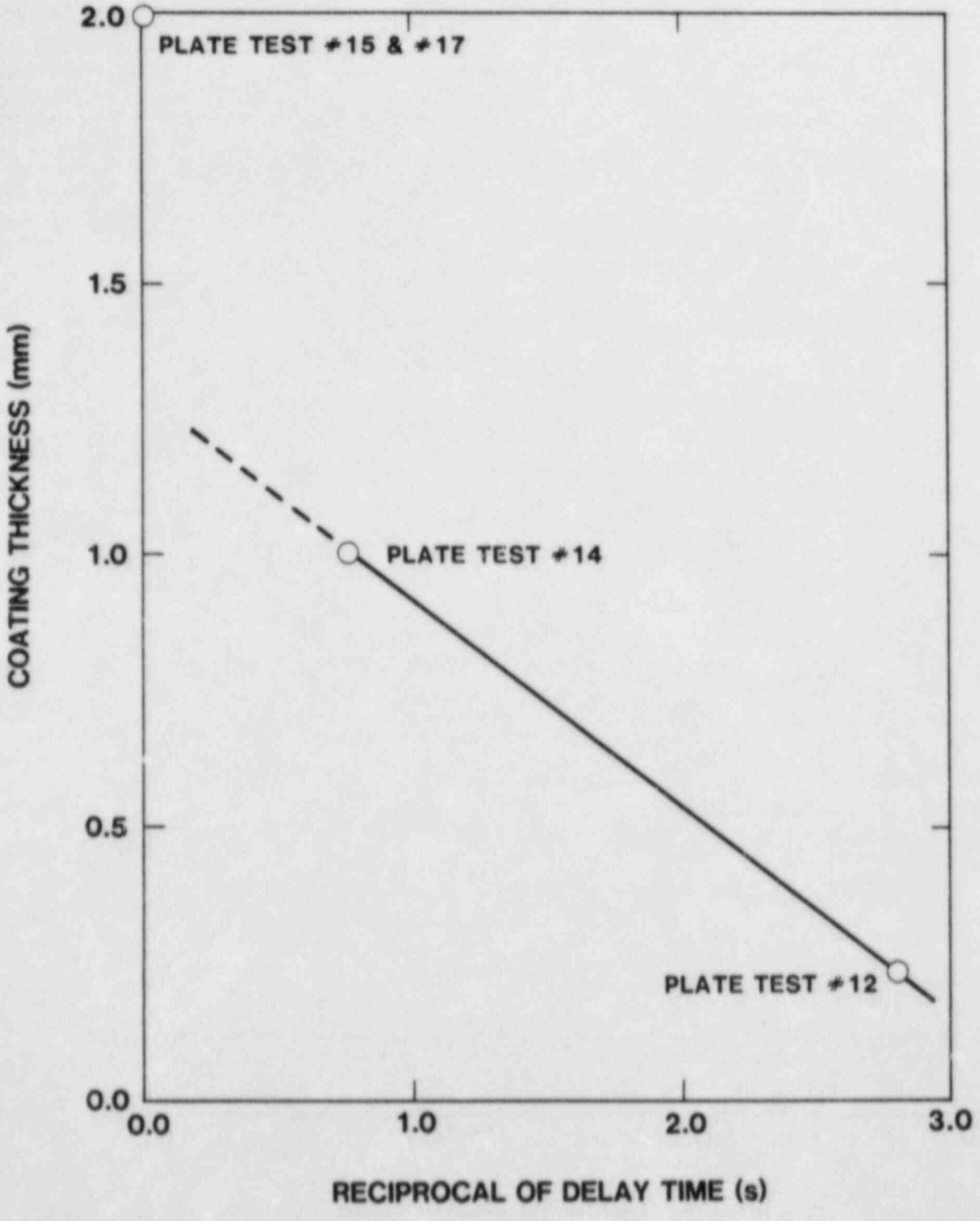

Figure 16. Reciprocal of the Delay Time Caused by Urania Coatings 0.23 to 2 mm Thick.

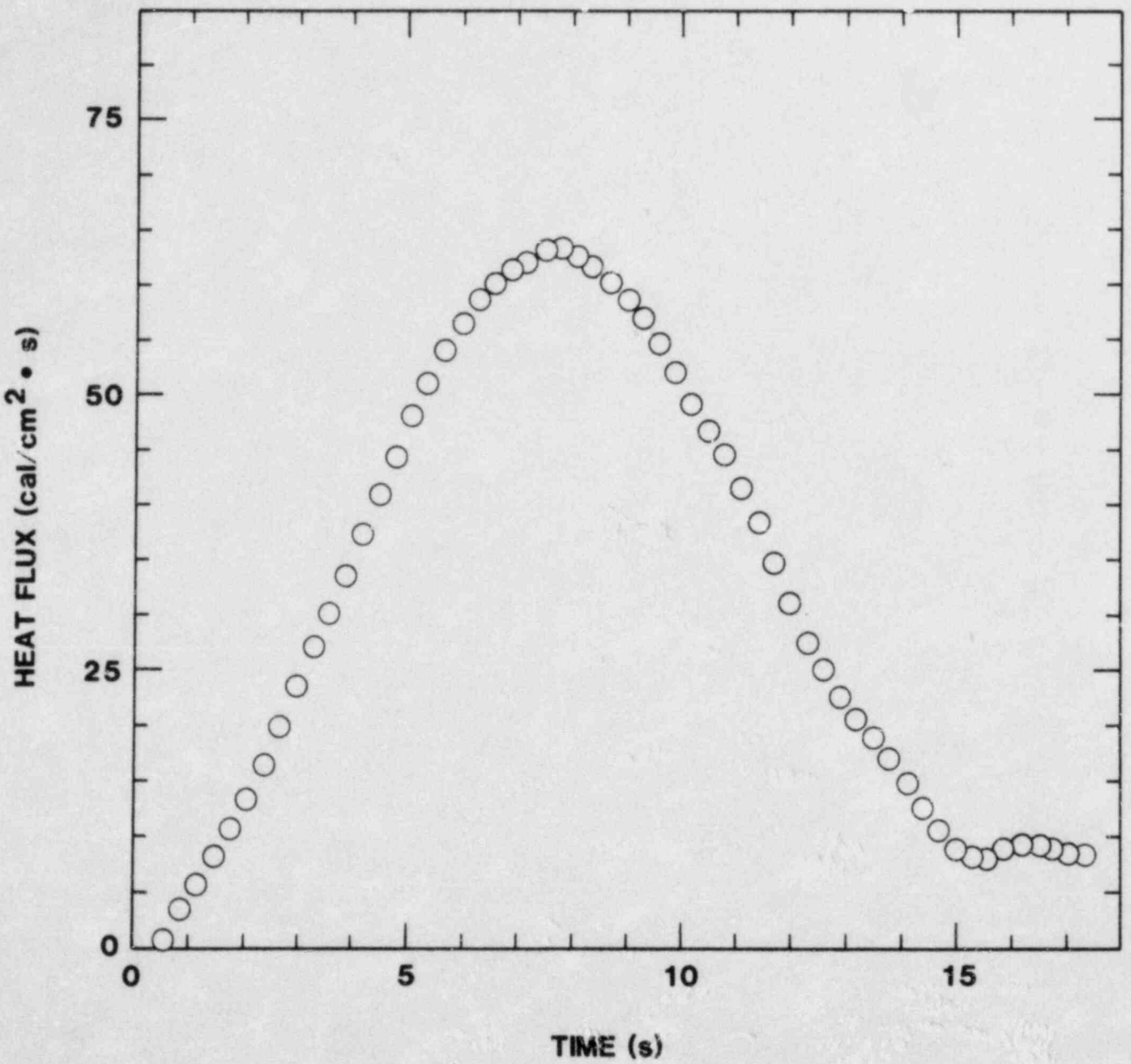

Figure 17. Heat Flux to the Steel in Test PLATE #15 Calculated by Inverse Heat Flux Analysis.

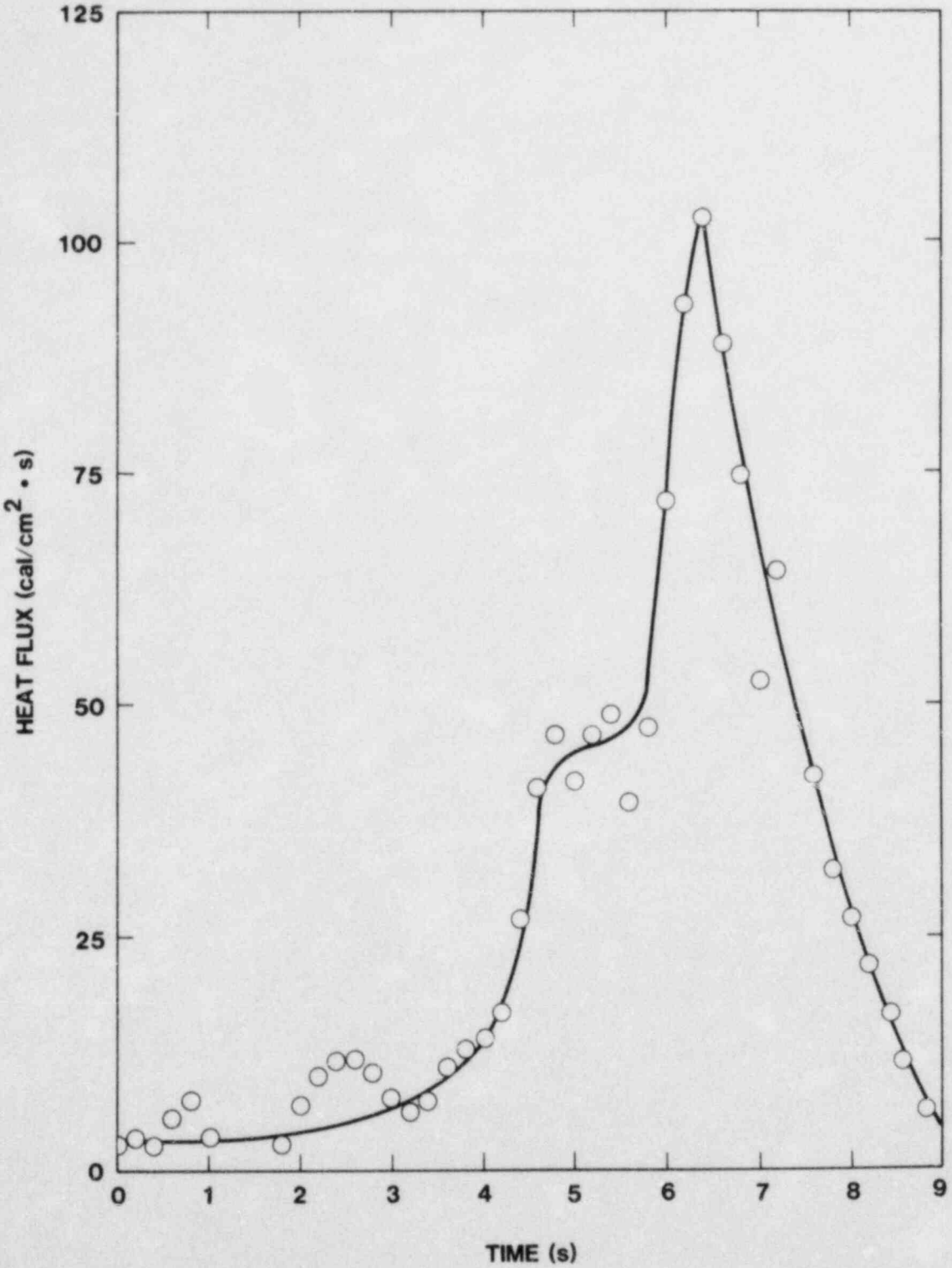

Figure 18. Heat Flux to the Steel in Test PLATE #17 Calculated by Inverse Heat Flux Analysis.

In test PLATE #15 a pool of melt was deliberately collected on the target plate as melt streamed from the crucible. The peak heat flux derived from temperatures measured on the unexposed surface of the plate came about 7 seconds after melt first hit the plate. This peak heat flux was found to be about 64 cal/cm^2-s. This is about a factor of forty less than that experienced by unprotected plates exposed to the direct action of the melt. This peak heat flux is about that produced by a quiescent melt in contact with steel (6). The heat flux decayed slowly. About 5 seconds were required before the flux had dropped to half its peak value.

In test PLATE #17 collection of a pool of melt was prevented. The peak heat flux at the urania interface with the steel plate developed about 6.4 seconds after melt first hit the target plate. The maximum heat flux was found to be 105 cal/cm^2-s. The inverse heat flux analysis probably yields a lower bound on the true heat flux for this case (see Appendix C). The flux decayed rapidly. About 1 second after this peak had been reached, the heat flux had fallen to half its peak value. The decay of the heat flux to the steel was smooth. The rise to the global maximum exhibited some intermediate maxima. Most of these are obviously the result of the inherent instability of inverse heat flux analysis. A shoulder in the heat flux at five seconds after the start of the test may be real but has not yet been explained.

If it is assumed that the maximum heat flux to the surface of the urania coating occurs at zero time, then the times of maximum heat flux at the coating interface with the steel in tests PLATE #15 and PLATE #17 imply thermal diffusivities for the coating of 0.00143 and 0.00156 cm^2/s, respectively. These values are consistent with what would be expected for the oxide coatings.

The inverse heat flux analysis shows how radically an oxide coating on the steel can delay and reduce the peak heat flux to the underlying steel. The analysis also shows that collection of a melt pool on the target plate reduces the heat flux probably by interfering with the hydrodynamics of the jet (4).

IV. GLOBAL CORRELATION OF PENETRATION DATA

Data obtained in the PLATE tests and in previous tests with lower temperature, furnace-prepared, melts (1) may be used to obtain a correlation of the time required for a melt stream to penetrate a steel structure in terms of:

(1) melt temperature,

(2) stream velocity, and

(3) steel structure thickness.

There are insufficient data to develop a correlation that addresses the effects of oxide coatings.

The correlation will strictly be applicable to steel or stainless steel melts streaming on steel structures. Evidence from the PLATE tests shows that both melt properties and structure properties should appear in the correlation. Theoretical and experimental correlations based on simulant fluids involve these properties. Only meager attempts to include structure properties will be made here. There are insufficient data available to include melt properties other than melt temperature. Since the melts used in the experiments that form the basis of the correlation are prototypic as are the structures exposed to the melts, the empirical correlation should still be useful for reactor safety analyses.

The data used to develop the correlation are assembled in Table V. Also shown in the table are uncertainties ascribed to the data. The plate thicknesses are taken to be exact in comparison to uncertainties in other quantities. Uncertainties in the time of penetration are taken to be 0.1 second. This is much greater than uncertainties in the measurements made in the experiments. But replication of the experiments would very likely yield outcomes that differ from those reported here by at least one tenth of a second.

Noticeably absent from the data list is mention of stream diameter. Stream diameter has been used in correlations of the type described here (5). It is, however, most difficult to understand why this parameter should be included. Its appearance in a correlation implies that a surface exposed to melt is affected by the amount of surface exposed to melt. This may be quite true near the perimeter of the melt stream. The analysis in Appendix C shows, however, that most of the exposed surface is unaffected by how large the stream is. Further, results of the PLATE tests suggest that previous uses of the geometric stream diameter may be incorrect. In reality some effective diameter which

is a function of the stream velocity should be used. Stream velocity is then the primal correlation variable. Finally, it was found unnecessary to include stream diameter to develop a satisfactory correlation.

Inspection of the data reported here and in reference 1 suggests a candidate correlation of the form:

$$t = \frac{\alpha_1(\alpha_2 + d)\rho Q\, V^{-\alpha_3}}{T_m - T_b}$$

where

t = time to penetrate the structure

d = thickness of the steel structure

Q = heat of ablation of the structure =

$$= \int_{T_o}^{T_b} C_p(T)\,dT + L$$

$C_p(T)$ = heat capacity of the structural material

L = latent heat of ablation

T_o = initial temperature of the structure

T_b = ablation temperature of the structure

T_m = bulk melt temperature

V = velocity of the melt

ρ = density of the structure material, and

α_1, α_2, and α_3 are parameters to be determined from experimental data.

The heat flux, q, and the coefficient of melt-to-structure heat transfer, h, derived from this correlation of penetration times are

$$q = \frac{(T_m - T_b)V^{\alpha_3}}{\alpha_1}$$

and

$$h = \frac{V^{\alpha_3}}{\alpha_1}$$

The parameter α_2 which appears in the correlation of time but not in the expressions above accounts for transient and non-thermal effects. When $\alpha_2 > 0$, it may be interpreted as meaning a crust of frozen melt forms on the structure. This crust must be remelted before erosion of the structure can begin. When $\alpha_2 < 0$ it may be interpreted as meaning mechanical processses such as creep-rupture contribute to the penetration of the structure.

Parametric values (α_1, α_2 and α_3) were obtained by non-linear least squares fitting of the experimental data to the correlation expression. The quality of the fits was judged by the parameter

$$X(P) = \sum_{i=1}^{N} (t_i(obs) - t_i(calc))^2/(N - P)$$

where

$T_i(obs)$ = observed penetration time

Table V. Data Used to Develop the Correlation

Penetration Time		Melt Stream Velocity		Temperature Difference		Plate Thickness**	Source
t(s)	γt*	V (cm/s)	γV	$T_m - T_b$ (^oC)	$\gamma(T_m - T_b)$	d (cm)	
0.98	0.1	143	20	1000	100	0.953	+
1.087	0.1	102	20	1000	100	0.953	+
0.759	0.1	255	30	1000	100	0.953	+
1.292	0.1	143	20	1000	100	1.270	+
1.933	0.1	143	20	1000	100	1.90	+
1.192[(a)]	0.1	143	20	1100	100	1.27	+
2.46	0.1	450	50	163	10	0.953	reference 1
10.5	0.1	430	30	163	10	3.00	reference 1
4.10	0.1	410	30	163	10	1.27	reference 1
20.42	0.1	410	30	163	10	6.12	reference 1

* γx = uncertainty in the quantity x

** Assumed to be exact

\+ This work

[(a)] stainless steel plate

T_i(calc) = calculated penetration time

N = number of data points used

P = number of parameters used in the fitting.

Fits were done with some of the parameters held at fixed values. The significance of an additional parameter was judged from the F statistic

$$\frac{X(P-1) - X(P)}{X(P)/(N-P)} = F$$

The critical value of the F-statistic is $F_c = F(\alpha, 1, N-P)$ at the 100 $(1-\alpha)$% confidence level.

Results of the various least-squares fittings are summarized in Table VI. Based on the F-test a correlation involving a single parameter, α_1, yields a satisfactory fit to the data if α_3 is set to 0.50 and α_2 is fixed at zero. The necessity of including α_2 or allowing α_3 to vary freely can be endorsed to a confidence level of much less than 90%. Inclusion of α_2 and α_3, while they do improve the fit to the data, was therefore deemed unnecessary.

Penetration times predicted with the single parameter correlation are compared to the experimentally determined penetration times in Table VII. The differences between predicted and observed times are all quite small--usually 0.1 to 0.2 seconds. On a percentage basis the errors are smallest for the longer penetration times. This is because the non-linear least-squares fitting procedure used to determine the parameter was set up to yield a uniform absolute error structure.

The authors conclude that because a satisfactory correlation could be obtained with $\alpha_2 = 0$, neither mechanical processes nor crust formation had significant effects on the rate of plate penetration in the tests. Further, the dependence on melt velocity is found to be consistent with a stagnation flow model if any effect of stream diameter is neglected.

Table VI. Results of Least-Square Fittings

Model	α_1	α_2	α_3	X(P)
1	7.9728	-0.0324	0.5932	0.75104
2	4.5366	-0.0174	$\equiv$0.5	0.83450
3	7.4334	$\equiv$0	0.5828	0.76844
4	4.518	$\equiv$0	$\equiv$0.5	0.83969

The symbol $\equiv$X means the parameter was held constant at the value X

Table VII. Comparison of Calculated and Observed Penetration Times

Observed Penetration time (s)	Calculated Penetration time (s)	Difference (s)
0.98	0.87	-0.11
1.087	1.029	-0.058
0.759	0.651	-0.108
1.292	1.163	-0.128
1.933	1.749	-0.184
1.192	0.967	-0.225
2.46	2.93	+0.47
10.50	9.86	-0.64
4.10	4.24	+0.14
20.42	20.67	+0.25

The effect of stream velocity on penetration time revealed by the combined data set from this and previous work is different from that shown by just the data reported here. This difference is probably not significant. It probably reflects the broader variation in melt velocity in the combined data set than the variation in data reported here.

The parameter, α_1, is a function of the data which are themselves uncertain. To determine the uncertainty in α_1 due to uncertainty in the data, the non-linear least squares fitting routine was repeatedly run with each datum allowed to randomly vary over its uncertainty range (see Table V). About 5000 repetitions were required to obtain a variance in α_1, stable to one part in 10^4. The uncertainty in α_1 was then found from

$$(\sigma_{\alpha_1})^2 = \sum(\alpha_1(i) - \bar{\alpha}_1)^2/(N - 1)$$

where

σ_{α_1} = uncertainty in α_1

$\alpha_1(i)$ = value of α_1 found on the i^{th} replication

N = number of replications

$\bar{\alpha}_1$ = mean value of α_1.

The correlation of penetration times is then

$$t = \frac{(4.518 \pm 0.103)\ d\rho Q\ V^{-1/2}}{(T_m - T_b)}$$

This correlation is based on a finte data set. The uncertainty in penetration time calculated when data assume the mean values in the data base is

$$\left(\frac{\gamma t}{t}\right)^2 = \left(\frac{\gamma\alpha}{\alpha}\right)^2 + \left(\frac{\gamma(T_m - T_b)}{(T_m - T_b)}\right)^2 + \frac{1}{4}\left(\frac{V}{\bar{V}}\right)^2$$

or

$$\left(\frac{\gamma t}{t}\right) \cong 0.120$$

where

$\gamma x \equiv$ the uncertainty in the quantity x.

For values of the data that differ from the mean values of the data base the uncertainty in an estimate of the penetration time from the correlation is given by

$$\sigma_t^2 = \gamma_t{}^2 \left[\frac{1}{10} + \frac{(d - 1.86)^2}{23.78} + \frac{(V^{-1/2} - 0.069)^2}{0.00354} + \frac{(T_m - T_b - 675)^2}{1.757 \times 10^6}\right] + (\gamma t)^2$$

In this, as in any empirical correlation, there is a severe loss in certainty when the correlation is extroplated beyond the data base used to derive the correlation. An estimate made with this correlation has 100(1-α)% confidence interval given by

$$\pm\ t(1-\alpha/2,9)\ \sigma_t$$

where $t(1-\alpha/2,9)$ is the student's t distribution for 9 degrees of freedom. Some useful values of the distribution are:

100 (1-α)%	$t(1-\alpha/2,9)$
99	3.69
95	2.82
90	2.62
80	1.83
60	1.38

Plots of the pentration time and associated confidence intervals against plate thickness, melt velocity, and melt temperature are shown in Figures 19, 20, and 21, respectively. Examination of these figures shows that validation of the empirical correlation would be best done with thick plates (~10 cm) and very high temperature melts (>2000°C). Development of a more broadly useful correlation would require experimental data involving lower temperature melts (<1600°C) that impact plates at low velocities (<100 cm/s).

These conclusions from the uncertainty analysis are readily interpretable. The experimental data base used to develop the correlation emphasizes conditions where quenching a crust on the steel at the point of melt impact is minimized. Consequently, validation of the correlation should be done with experiments that also involve these conditions. When melts are low in temperature and impact the steel at low velocities the thermal conditions for the transient existence of a quench layer exist and the heat fluxes are sufficiently low that the quench layer will last for sufficient time to delay penetration significantly. Experiments involving these conditions will involve phenomena not reflected in the data base used to develop the correlation. Consequently results of the experiments would be useful for development of a new correlation with a broader range of applicability.

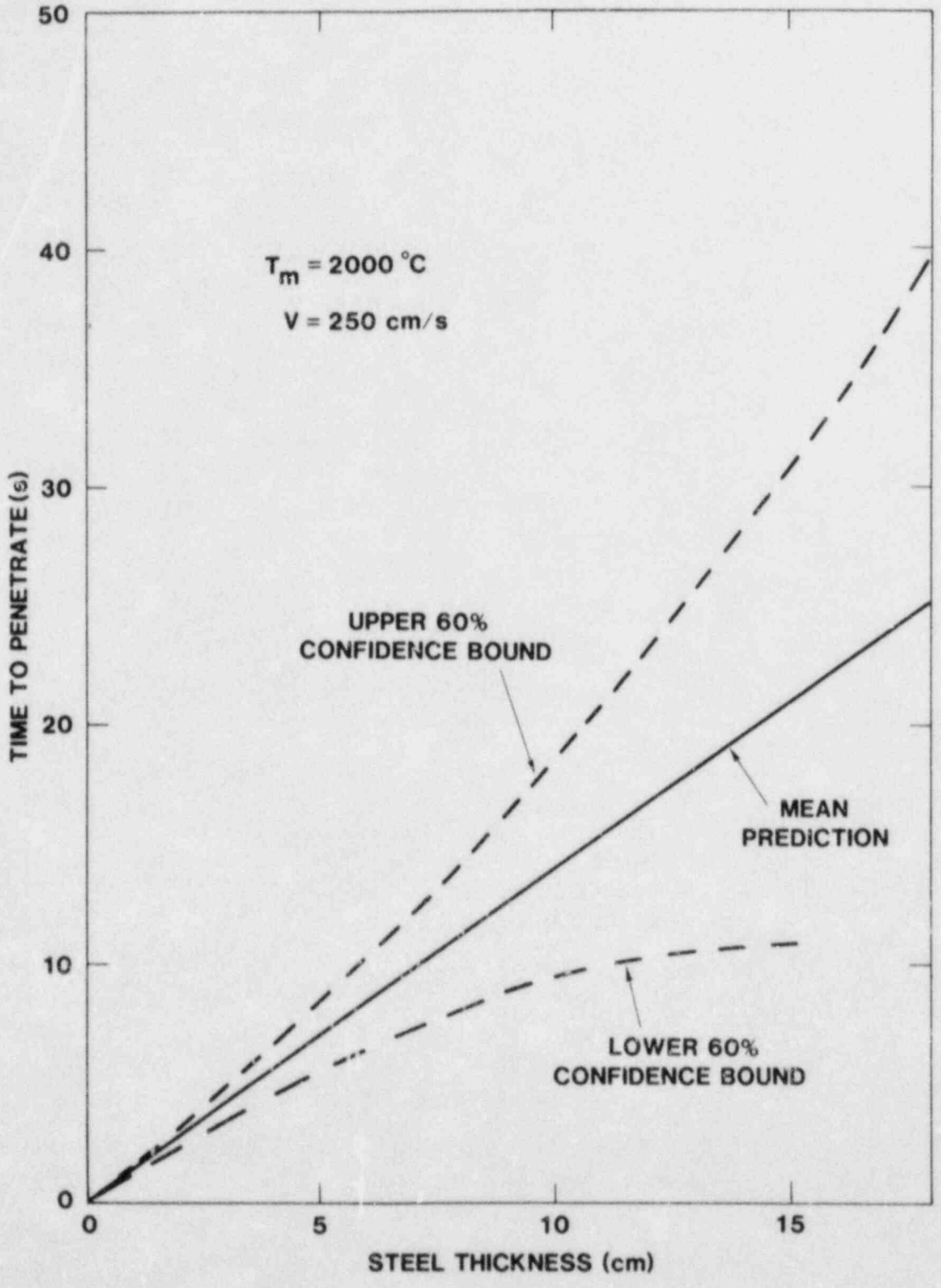

Figure 19. Time Required to Penetrate Steel Plates of Various Thicknesses by 2000°C Melts that Impact the Plates at 250 cm/s.

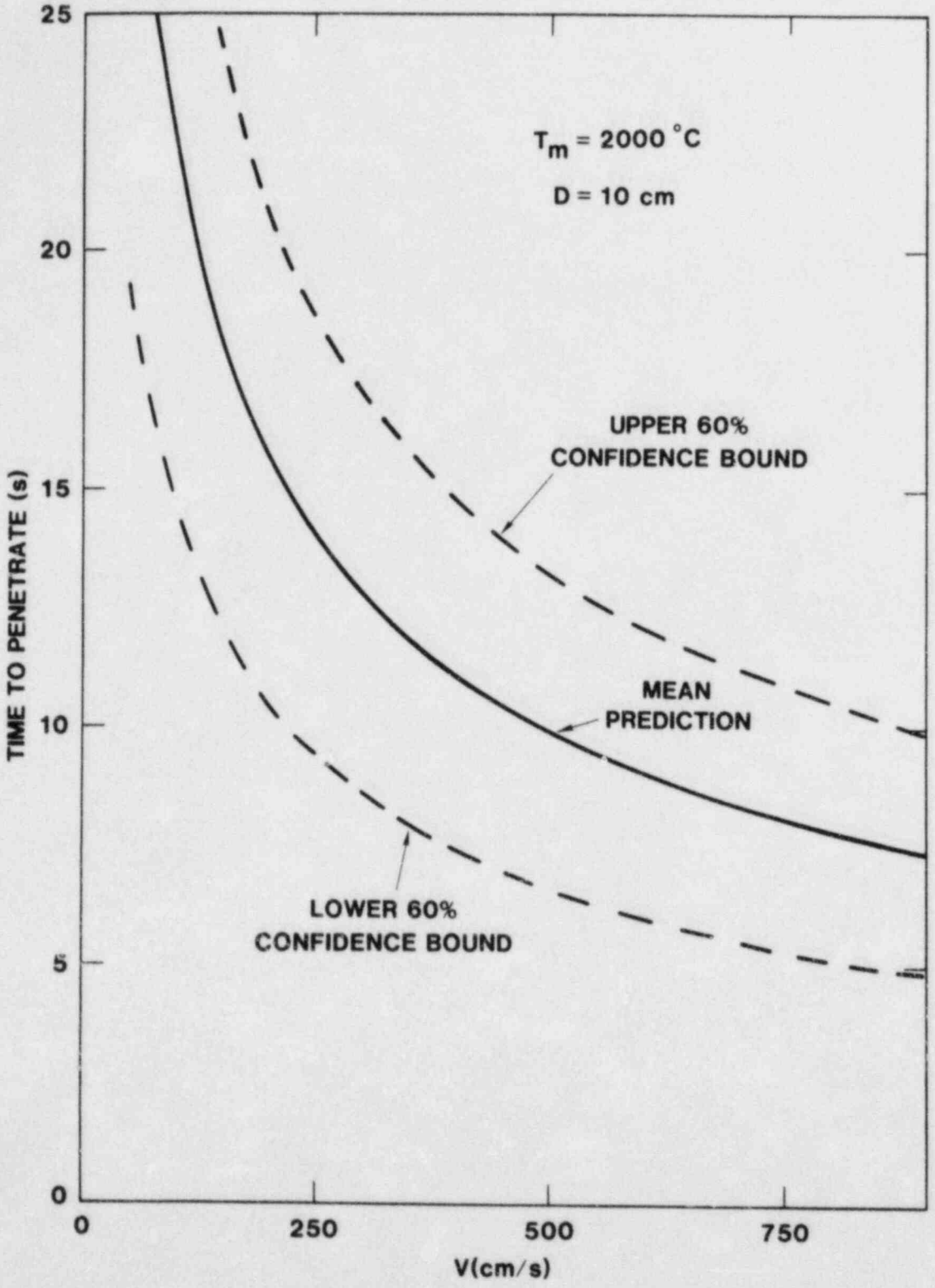

Figure 20. Time Required to Penetrate a 10 cm Thick Steel Plate by a 2000°C Melt that Impacts the Plates at Various Velocities.

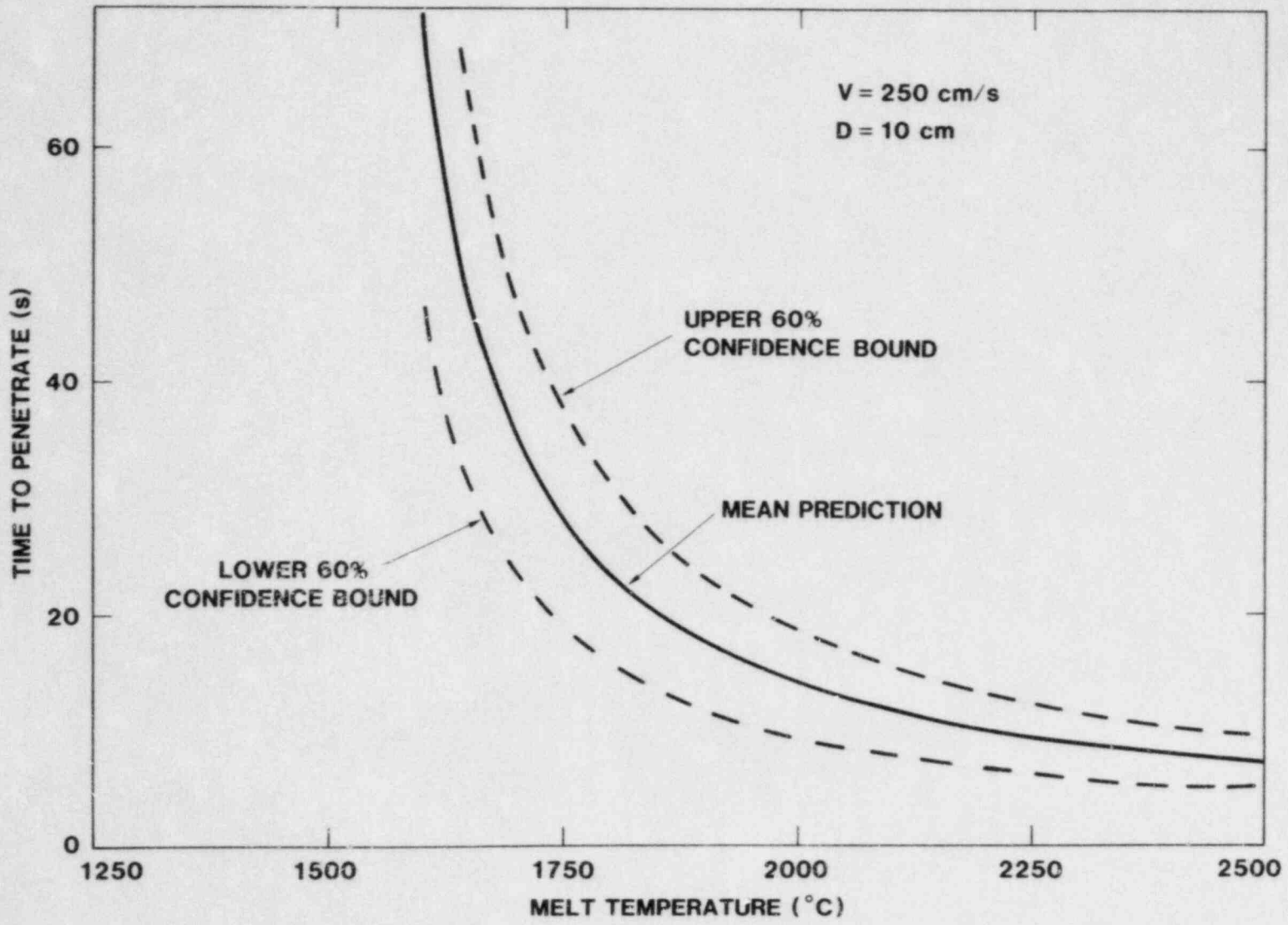

Figure 21. Time Required to Penetrate a 10 cm Thick Steel Plate by Melts of Various Temperatures that Impact the Plate at 250 cm/s.

References:

(1) D. A. Powers and F. E. Arellano, Erosion of Steel Structures by High Temperature Melts, NUREG/CR-2284; SAND81-1755, Sandia National Laboratories, Albuquerque, NM 87185.

(2) D. A. Powers and F. E. Arellano, Direct Observation of Melt Behavior During High Temperature Melt/Concrete Interactions, NUREG/CR-2283; SAND81-1754, Sandia National Laboratories, Albuquerque, NM 87185, January 1982.

(3) A. Le Clerc, LaHouille Blanche 5 816-821 (1950).

(4) M. M. Chen, "Erosion of a Low Melting Solid by a Hot Fluid Jet of Normal Incidence" preprint of a paper submitted to the AICHE 17th National Heat Transfer Conference, pp 166-175, 1977

(5) S. Sithanamayya and K. Subba Raju, Canad. J. Chem. Eng. 47, 365 (1969).

(6) D. M. Lewis and J. Savage, Met. Rev 1 (Part I) 65 (1956).

APPENDIX A

Maximum Temperatures During Corium Metallothermic Reactions

Reactor core melts will consist of mixtures of UO_2, ZrO_2, and stainless steel. The metallothermic reaction used in test PLATE #16 was designed to produce a melt similar to a reactor core melt. The ideal composition of the thermitically-produced melt is 54 w/o UO_2, 16 w/o ZrO_2 and 30 w/o stainless steel.

Calculated, standard-state, adiabatic reaction temperatures have been shown to be surprisingly accurate estimates of maximum temperatures realized in classic thermite reactions (1). The estimates calculated this way are most useful when the possibility of incomplete reaction is recognized and the latent heat effects of phase transitions are included. An adiabatic reaction temperature analysis of the corium metallothermic reaction is presented in this appendix. Latent heat effects are included in the analysis. An approximate treatment of incomplete reactions is attempted.

The constituents of the charge for the corium metallothermic reaction are listed in Table A-1. Stainless steel powder is included in the charge so that the final product of reaction has the desired metal content. This powder does not contribute to the energy yield of the reaction. It does absorb heat produced by the reaction.

The adiabatic temperature analysis is begun by computing the heat yield of the reactions as though they occurred at room temperature (298 K). The effect of incomplete reaction may be approximated by assuming the fuels in the corium charge (Zr and U) are contaminated by some of their respective oxides. The formal stoichiometries of the major heat-generating reactions in the charge are then:

Reaction 1: $\Delta H_1 = 251.1$ Kcal/mole

$$2(1-\varepsilon)U + 2\varepsilon UO_2 + Fe_3O_4 \longrightarrow 2UO_2 + 3(1-\varepsilon)Fe + \varepsilon Fe_3O_4$$

Reaction 2: $\Delta H_2 = 259.3$ Kcal/mole

$$2(1-\alpha)Zr + 2\alpha ZrO_2 + Fe_3O_4 \longrightarrow 2ZrO_2 + 3(1-\alpha)Fe + \alpha Fe_3O_4$$

Reaction 3: $\Delta H_3 = 250.0$ Kcal/mole

$$1.5(1-\varepsilon)U + 1.5\varepsilon UO_2 + CrO_3 \longrightarrow 1.5UO_2 + (1-\varepsilon)Cr + \varepsilon CrO_3$$

Table A-1. Constituents of the Corium Metallothermic Reaction Mixture

Constituent	Weight (g)	Moles
	REACTION MIXTURE	
U	0.475	0.0020
Zr	0.11845	0.00139
Fe_3O_4	0.29997	0.00130
NiO	0.029861	0.00040
CrO_3	0.101537	0.00102
Stainless Steel	0.006681	-
	IDEALIZED PRODUCTS	
UO_2	0.540	0.0020
ZrO_2	0.160	0.00130
Fe	0.222	0.0040
Cr	0.054	0.00104
Ni	0.024	0.00041

Reaction 4: $\Delta H_4 = 256.15$ Kcal/mole

$$1.5(1-\alpha)Zr + 1.5\alpha ZrO_2 + CrO_3 \longrightarrow 1.5ZrO_2 + (1-\alpha)Cr + \alpha CrO_3$$

Reaction 5: $\Delta H_5 = 72.0$ Kcal/mole

$$0.5(1-\varepsilon)U + 0.5\varepsilon UO_2 + NiO \longrightarrow 0.5UO_2 + (1-\varepsilon)Ni + \varepsilon NiO$$

Reaction 6: $\Delta H_6 = 74.05$ Kcal/mole

$$0.5(1-\alpha)Zr + 0.5\alpha ZrO_2 + NiO \longrightarrow 0.5\ ZrO_2 + (1-\alpha)Ni + \alpha NiO$$

The ΔH_i values listed above are the heat yields per mole of oxide reactant assuming no contamination of the metallic reactant.

Uranium and zirconium are charged into the reaction mixture by weight assuming no contamination to provide the required amount of UO_2 and ZrO_2 in the final reaction product. Thus,

$$\frac{\text{"weight (U)"}}{\text{"weight (Zr)"}} = \frac{0.476}{0.11845} = \beta$$

But because of the contamination, actually

$$\beta = \frac{\text{moles (U)}\ (238 + 270\varepsilon/(1-\varepsilon))}{\text{moles (Zr)}\ (91.22 + 123.22\alpha/(1-\alpha))}$$

For the calculations presented here it was assumed $\alpha = \varepsilon$. Thus

$$\eta = \frac{\text{moles (U)}}{\text{moles (Zr)}} = \left[\frac{91.22(1-\varepsilon) + 123.22\varepsilon}{238(1-\varepsilon) + 270\varepsilon}\right]\beta$$

The heat yield from the reaction mixture is:

$$H(MIX) = \frac{(1-\varepsilon)}{(1+n)}\Big[\text{moles}(Fe_3O_4)(\Delta H_2 + n\Delta H_1) +$$

$$+ \text{moles}\ (CrO_3)(\Delta H_4 + n\Delta H_3) +$$

$$+ \text{moles}\ (NiO)\ (\Delta H_6 + n\Delta H_5)\Big]$$

In formulating this expression, alloying effects have been neglected. Also, the reactions are assumed to go in stoichiometric proportion.

The second step in the analysis is to compute the heat costs associated with raising the temperature of the reaction products and diluents. The costs for each species are given by

$$L_i(T) = \int_{298}^{T} C_p^{(i)}(T)dT + \sum_{j=1}^{N} \phi_i(T)$$

where

C_p = heat capacity

$\phi(T)$ = latent heat of phase transitions.

Latent heat effects are included only when the temperature exceeds the phase transition temperature.

For the analysis presented here the heat capacity integrals were approximated as linear functions of temperature. Further, since it was known that the reaction products would be liquids, latents heats of phase changes in the condensed products of reaction were incorporated in the constant terms of the linear approximation. Thus,

$$\int_{298}^{T} C_p^{(i)}(T)dT + \sum_{\text{condensed}} \phi_i(T) = \alpha_i + b_i T$$

Table A-2. Parameters for the Temperature Rise Calculations

Species	a_i	b_i
UO_2	-8893	31.3
ZrO_2	10770	21.0
Fe_3O_4	20276	48
Fe	-1890	10.8
CrO_3	480	19.7
Cr	1033	9.4
NiO	6425	14.9
Ni	-2268	9.4

Values used for the parameters a_i and b_i are listed in Table A-2.

This treatment of the heat costs of raising the temperature of the reaction products makes it necessary to be concerned only about condensed-to-vapor phase changes. Most of the oxide products are quite refractory and boil at temperatures above 3500 K. Chromic oxide (CrO_3) is an exception. It boils at about 1200 K. Heat associated with boiling CrO_3 (25 Kcal/mole) was included in the linear loss terms described above.

Metallic products of reaction boil at more modest temperatures as shown by the data in Table A-3. All of the metallic reaction products are completely miscible when liquid. The boiling of the metal phase is affected by this mutual solubility. An ideal solution approximation was made to determine the "boiling" point of the metal alloy. The alloy boils when the sum of the partial pressures of the constituents of the alloy reach the ambient pressure which for tests in the PLATE series was about 0.83 atmospheres. The partial pressure of the i^{th} constituent of the alloy is given by

$$P_i = X_i \exp(-\Delta G_i/RT)$$

where

P_i = partial pressure of species i

X_i = mole fraction of species i in the alloy

ΔG_i = free-energy of the condensed-to-vapor phase change for species i

R = gas constant

T = absolute temperature.

Temperature dependent functions that describe the free-energy of the condensed-to-vapor phase change are shown in Table A-3.

Table A-3. Vaporization of Metals

Metal	Boiling Point (K)	$H_{vap.}$ Kcal/mole	Free-energy of vapor formation cal/mole
Fe	3148	98.9	86467 - 27.45 T
Cr	2938	92.3	81974 - 27.92 T
Ni	3159	102.2	92836 - 29.43 T

Solving the equation

$$\sum_{i=1}^{3} P_i - 0.83 = 0$$

for temperature yields the "boiling" point of the alloy and the vapor composition. For the stainless steel alloy produced by the corium metallothermic reaction, the "boiling" point was found to be 3049K and the vapor composition was found to be:

55.9 a/o Fe

38.7 a/o Cr

5.4 a/o Ni

Notice that the vapor composition is quite different from the liquid composition. As vaporization progresses the vapor composition and the "boiling" point changes. The effective heat of vaporization is 97.3 Kcal per mole of vapor.

Solving the equation

$$\sum_{\text{products}} m(i)\ L(i) + S = H_{MIX}(\varepsilon)$$

where

S = 0 for T < 3049K

S = 97.3 Kcal/mole stainless steel for T > 3049K

yields the maximum adiabatic reaction temperature. Solutions for values of ε between about 0.6 and 0 are plotted in Figure A-1. For ε less than about 0.25, reaction temperatures are arrested by the boiling of steel. There is insufficient heat from the reaction to boil the steel completely. Over a broad range of reaction mixture compositions the maximum adiabatic temperature will be about 3050 K.

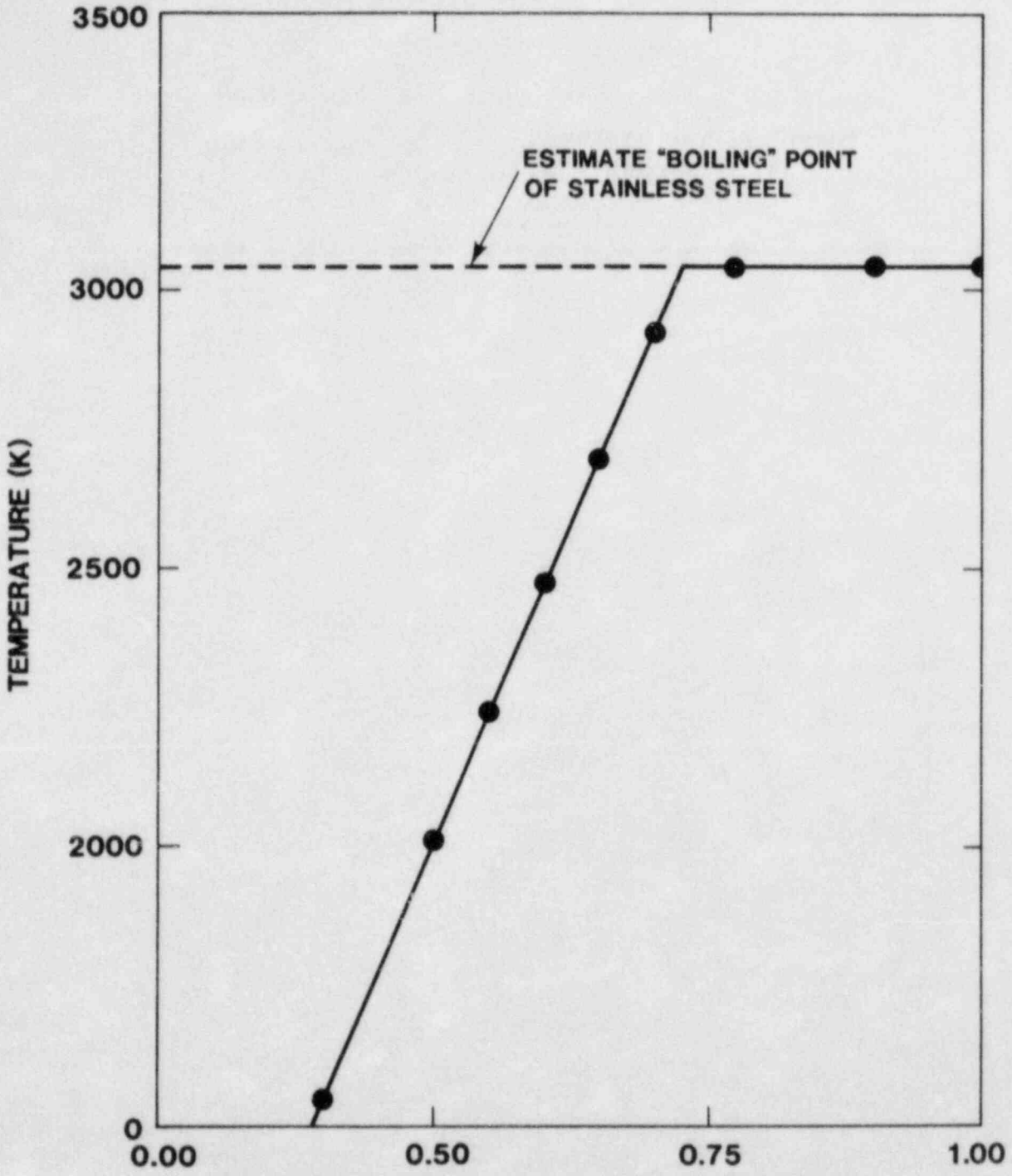

Figure A-1. Effect of Contamination or Incomplete Reaction on the Maximum Temperature of "Corium" Metallothermic Reactions.

APPENDIX B

Temperature Data from the PLATE Tests

Temperature data obtained from thermocouples welded to the back, unexposed, sides of the target plates are presented in Figures B-1 to B-12. The errors attributed to the temperature data are typical of thermocouple (1%) at temperatures below about 200°C. The rapid excursion in temperature just prior to penetration is less accurately recorded by thermocouple sensors. No attempt to determine the temperature uncertainties during the rapid excursion has been made.

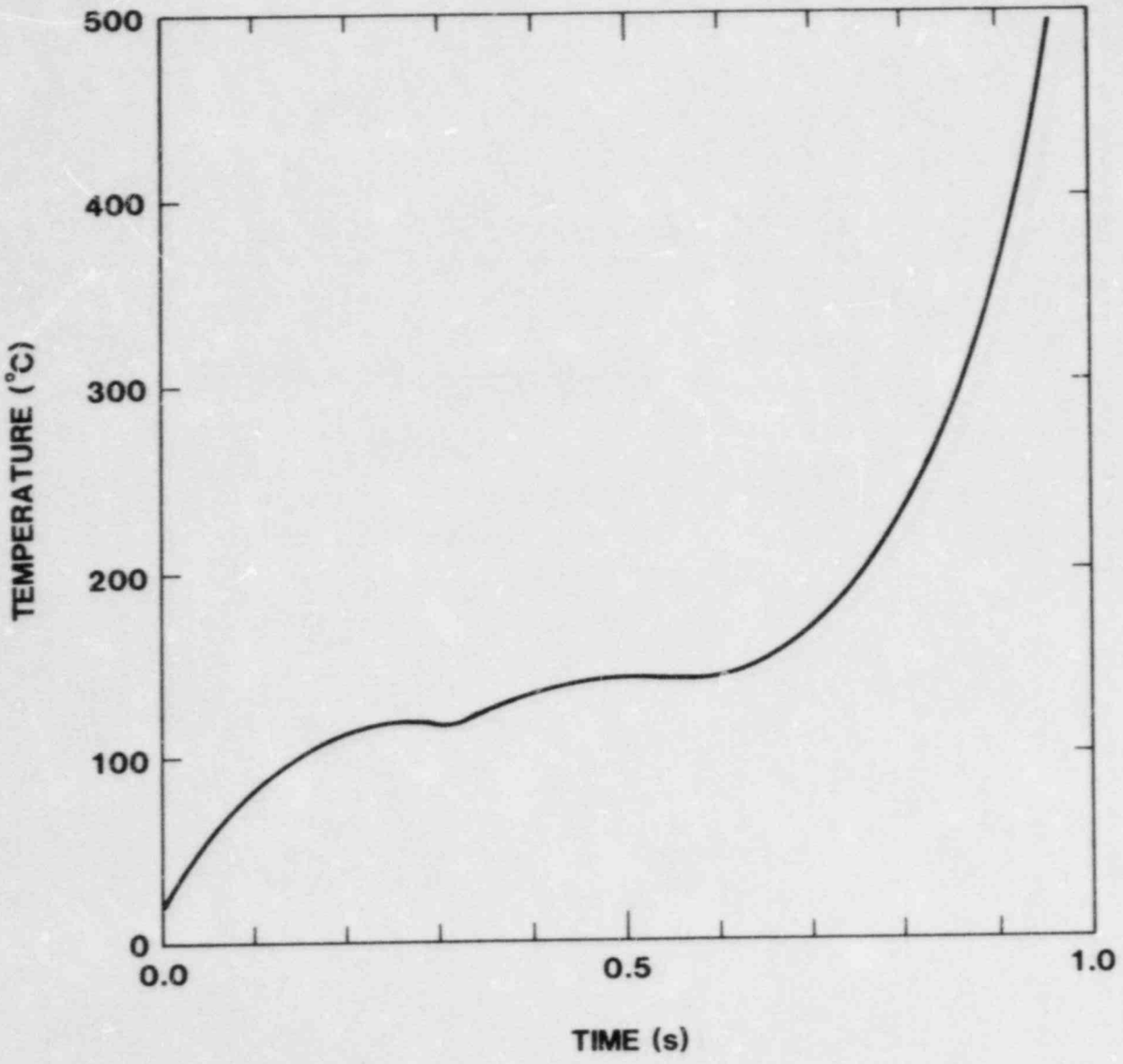

Figure B-1. Temperature Data from Test PLATE #5.

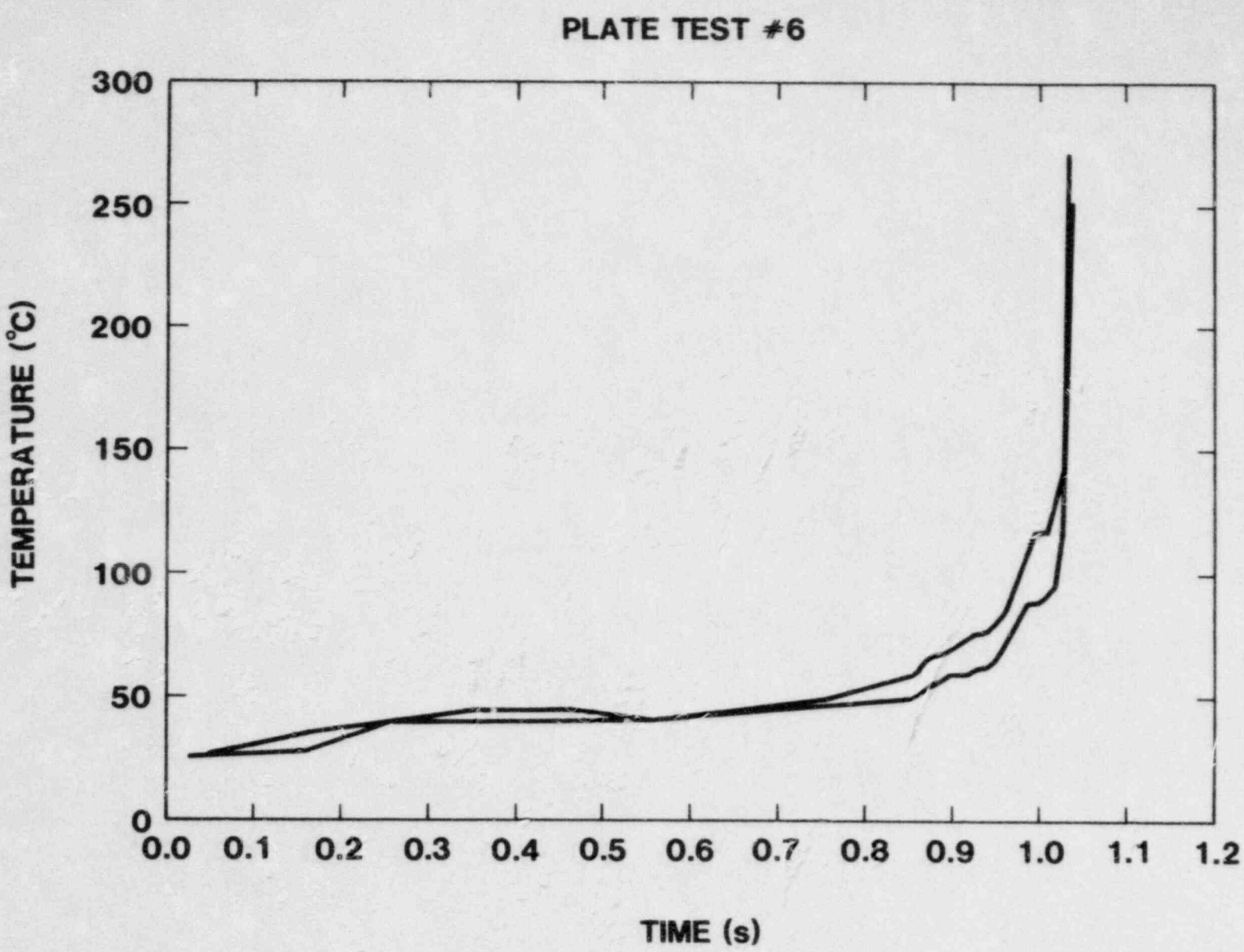

Figure B-2. Temperature Data from Test PLATE #6.

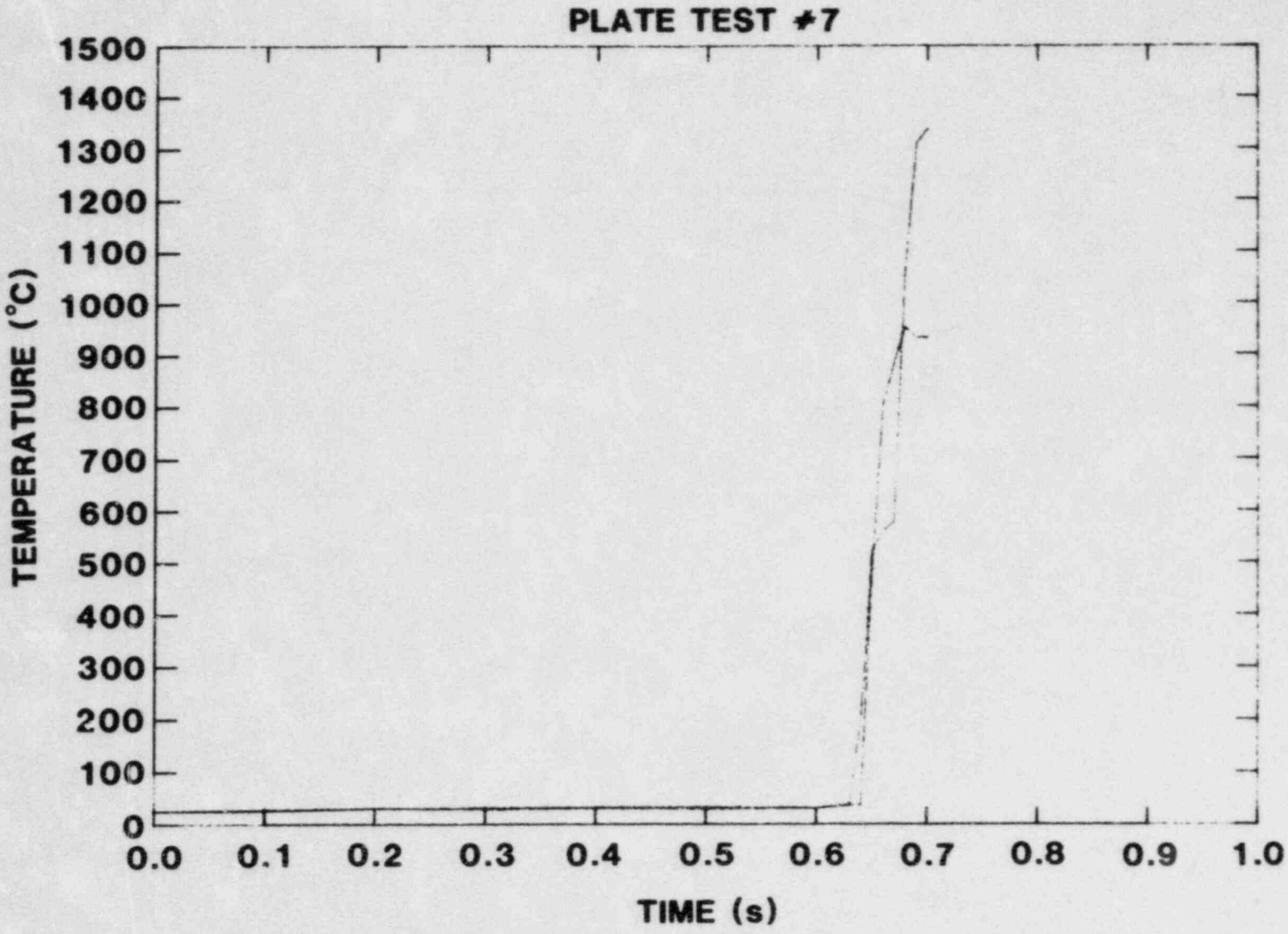

Figure B-3. Temperature Data from Test PLATE #7.

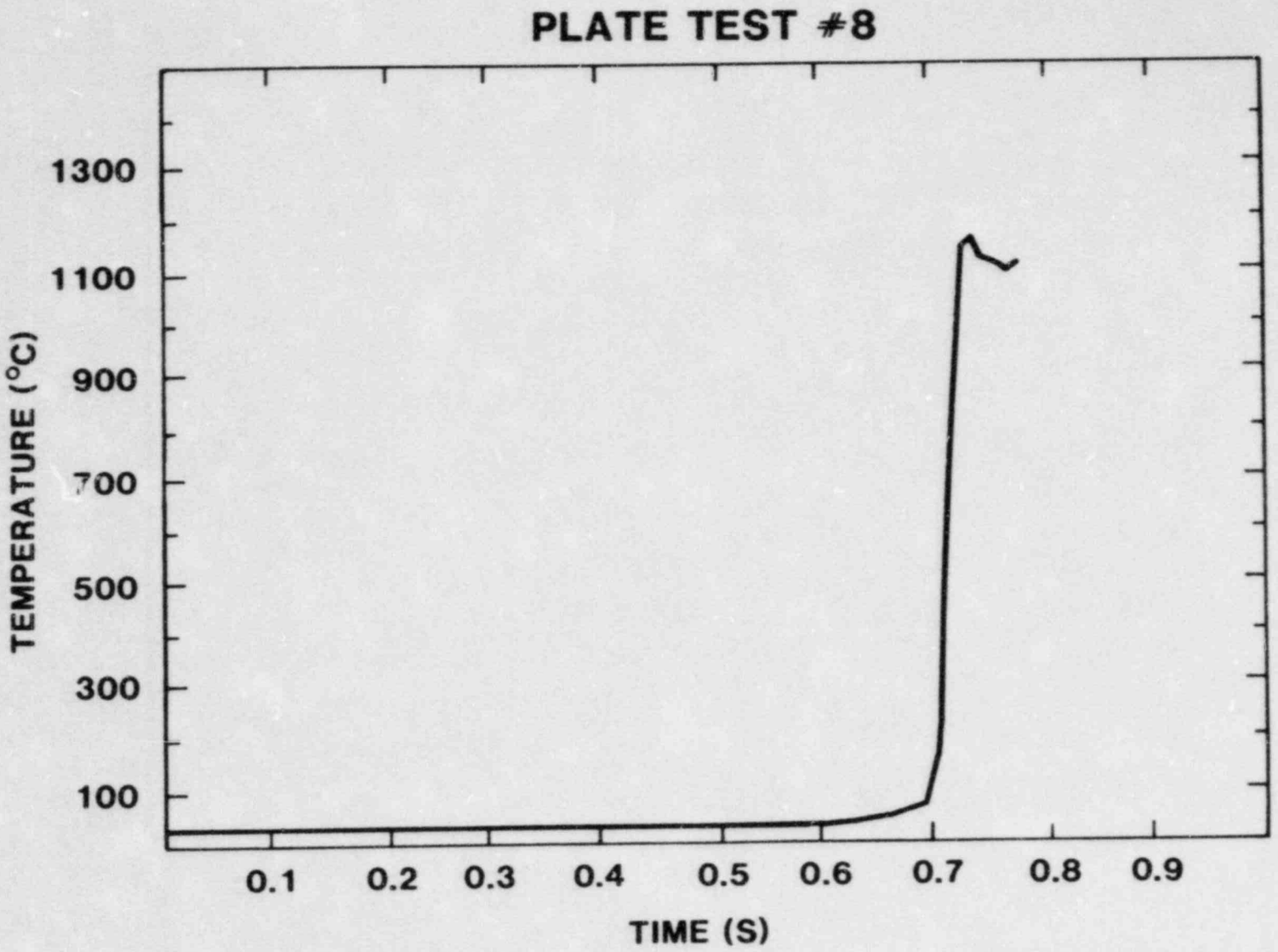

Figure B-4. Temperature Data from Test PLATE #8.

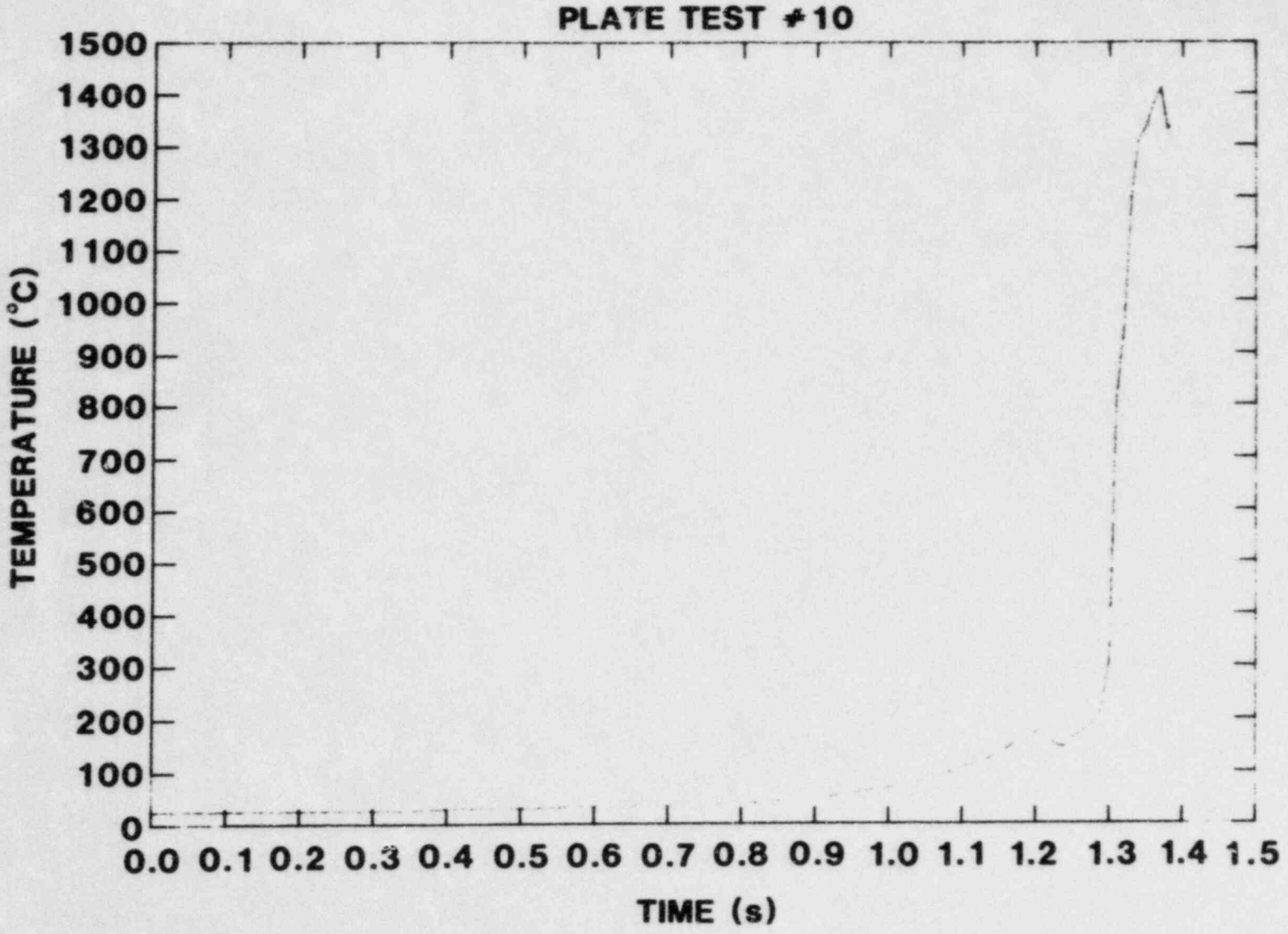

Figure B-5. Temperature Data from Test PLATE #10.

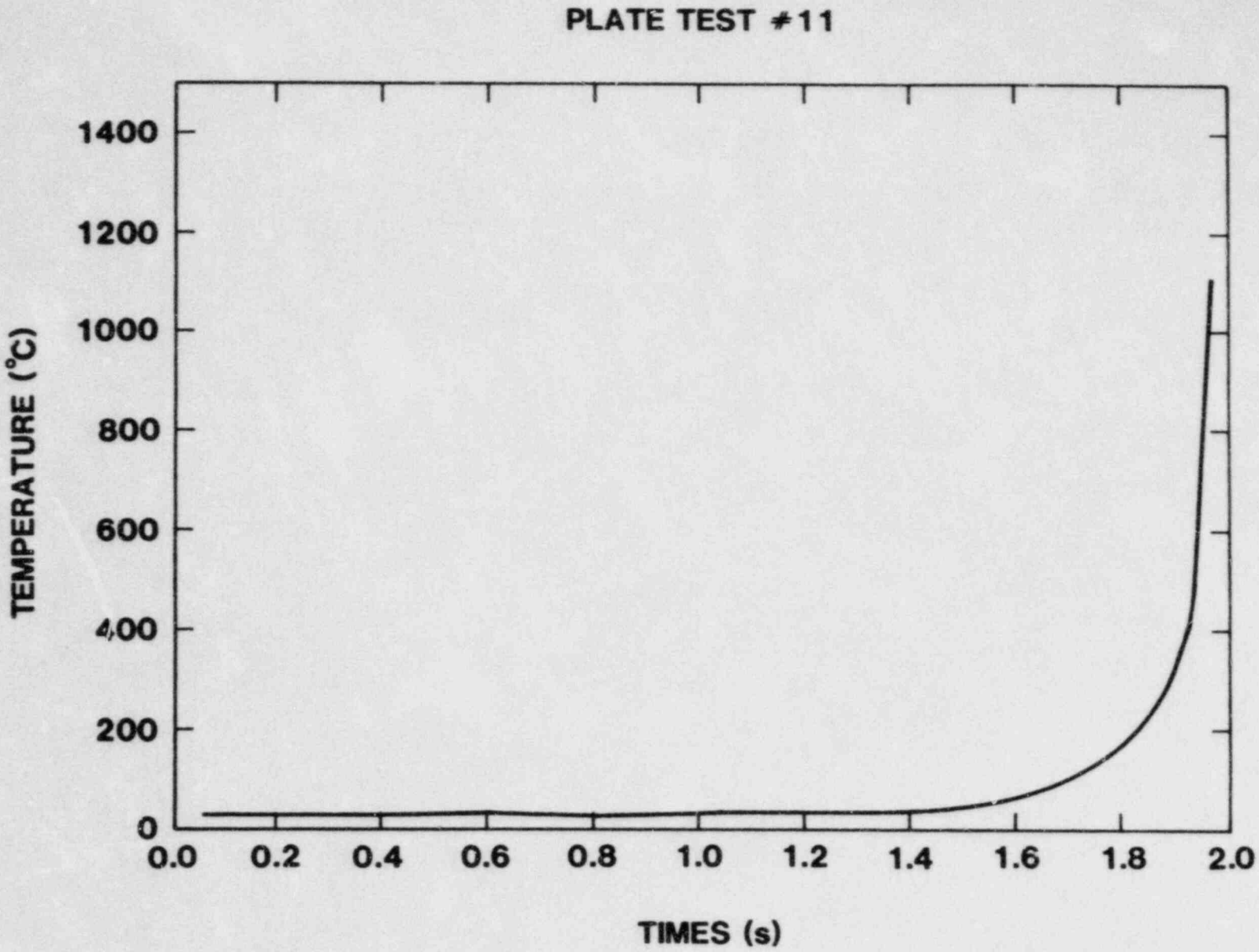

Figure B-6. Temperature Data from Test PLATE #11.

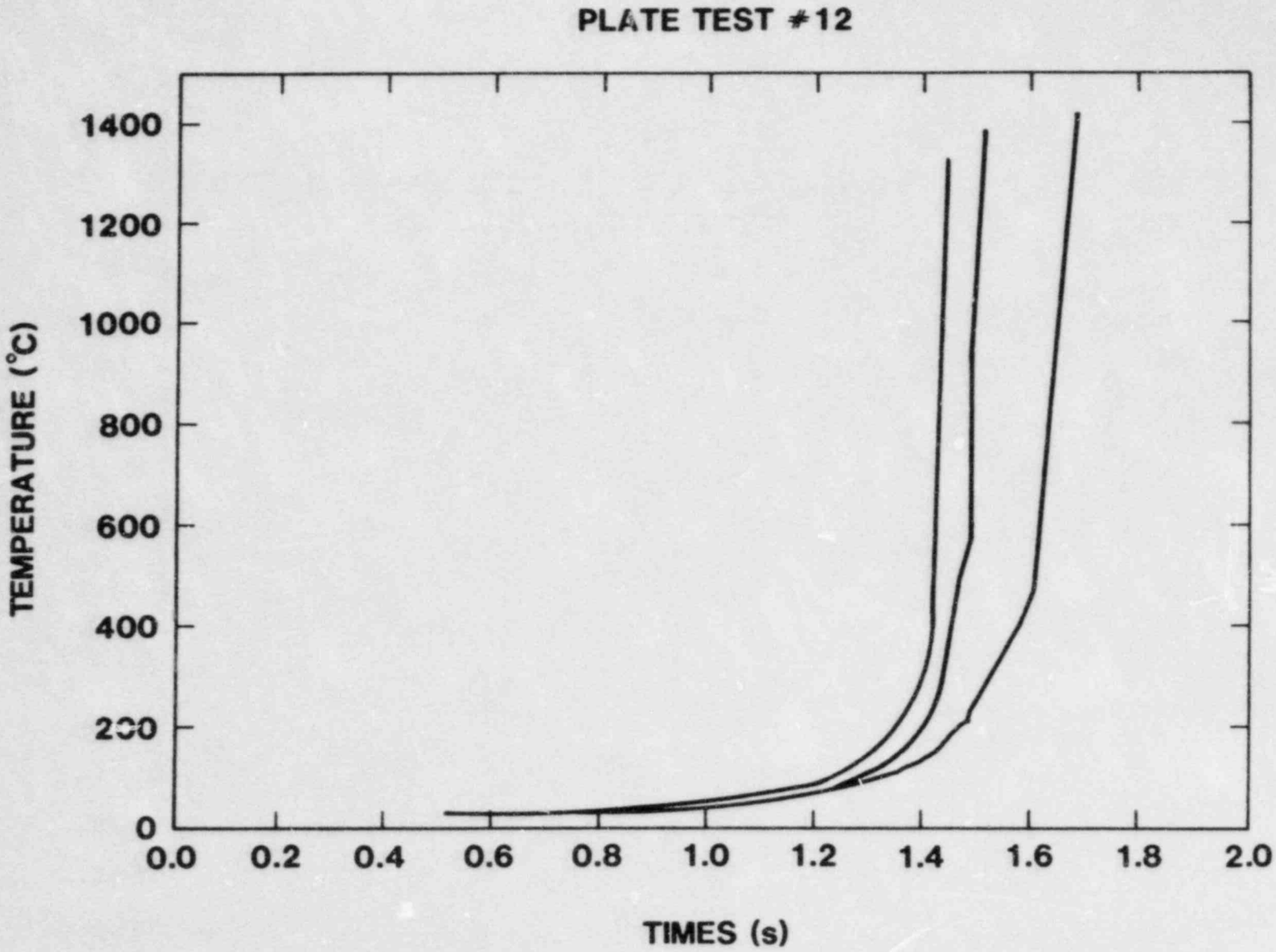

Figure B-7. Temperature Data from Test PLATE #12.

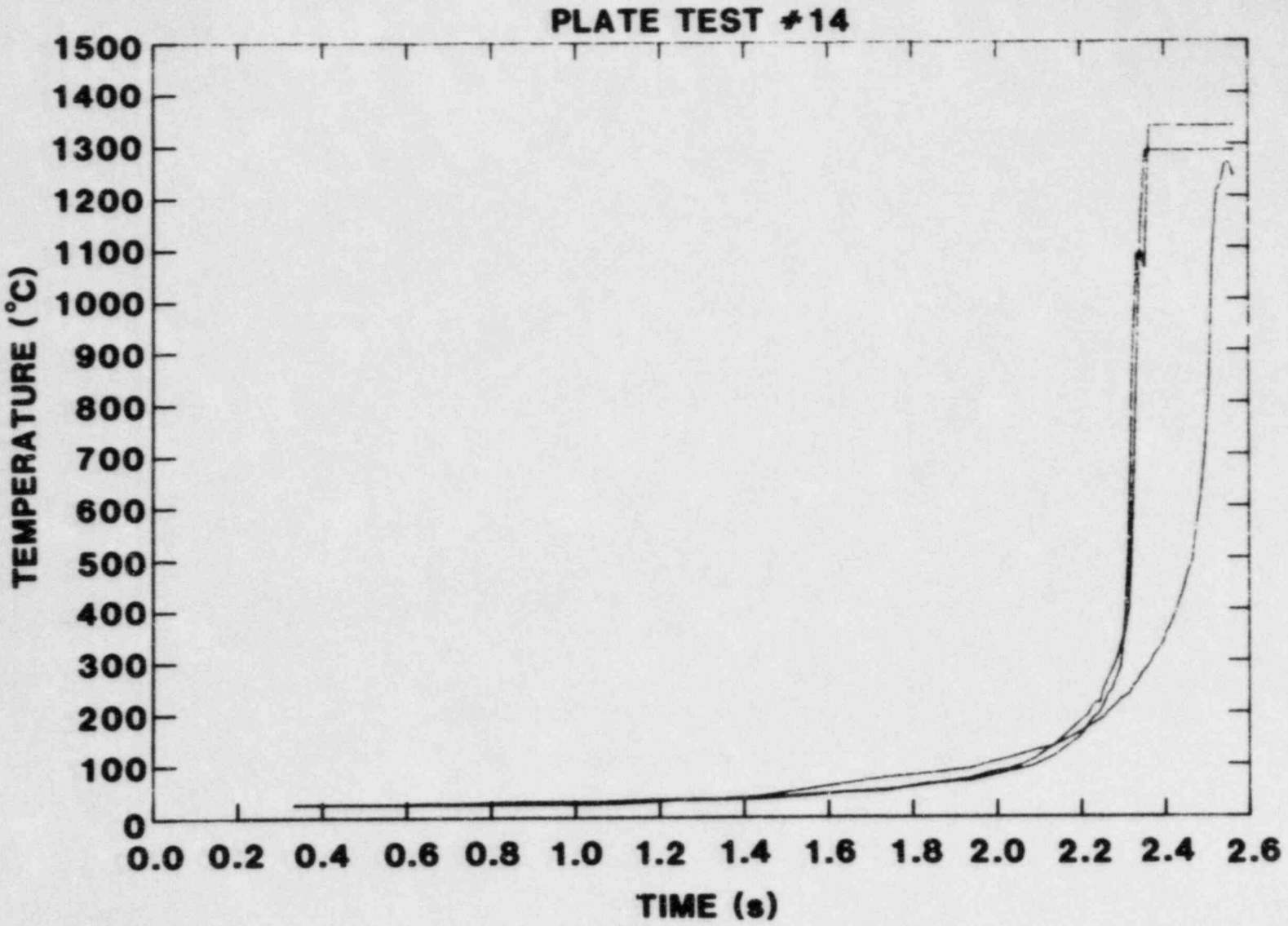

Figure B-8. Temperature Data from Test PLATE #14.

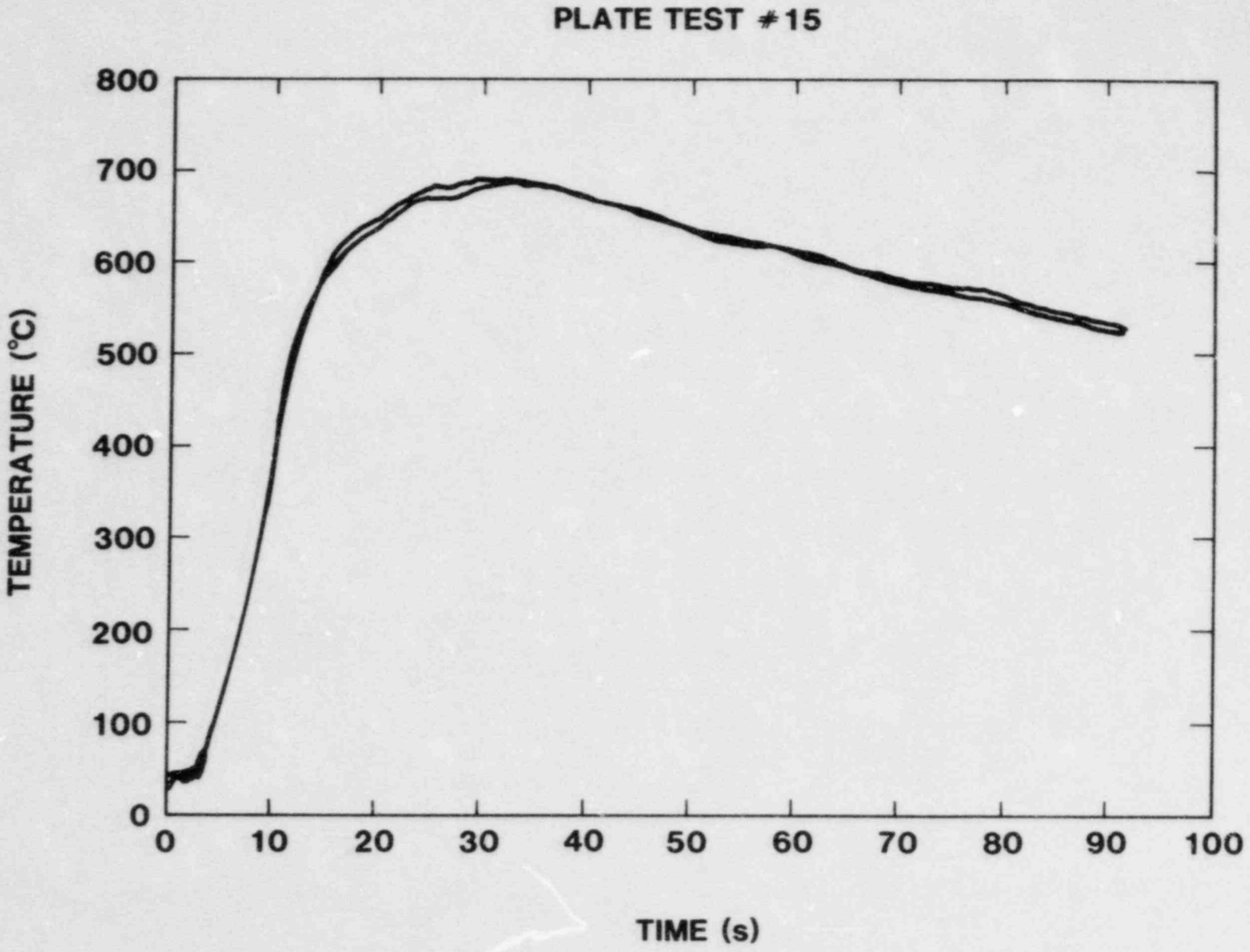

Figure B-9. Temperature Data from Test PLATE #15.

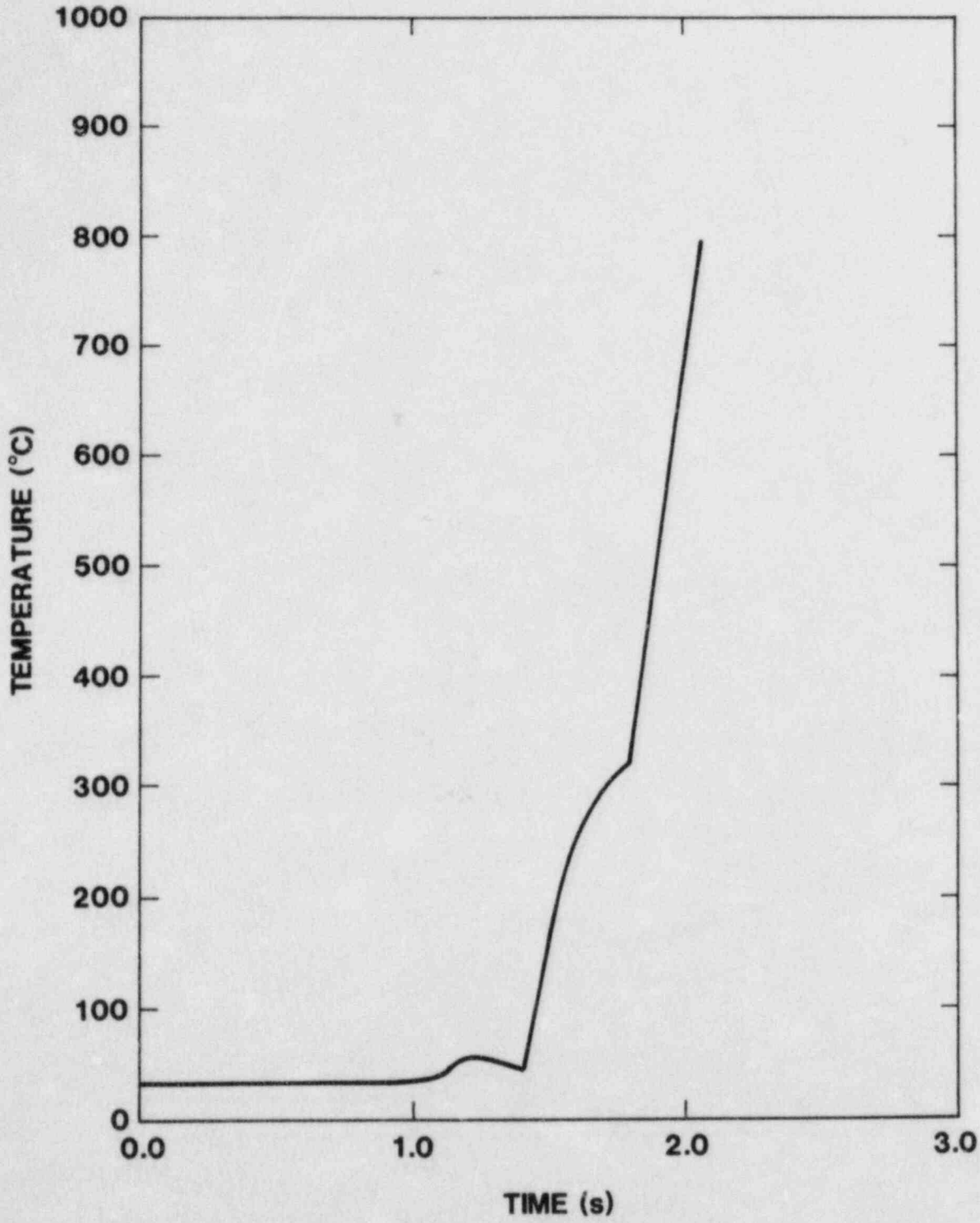

Figure B-10. Temperature Data from Test PLATE #16.

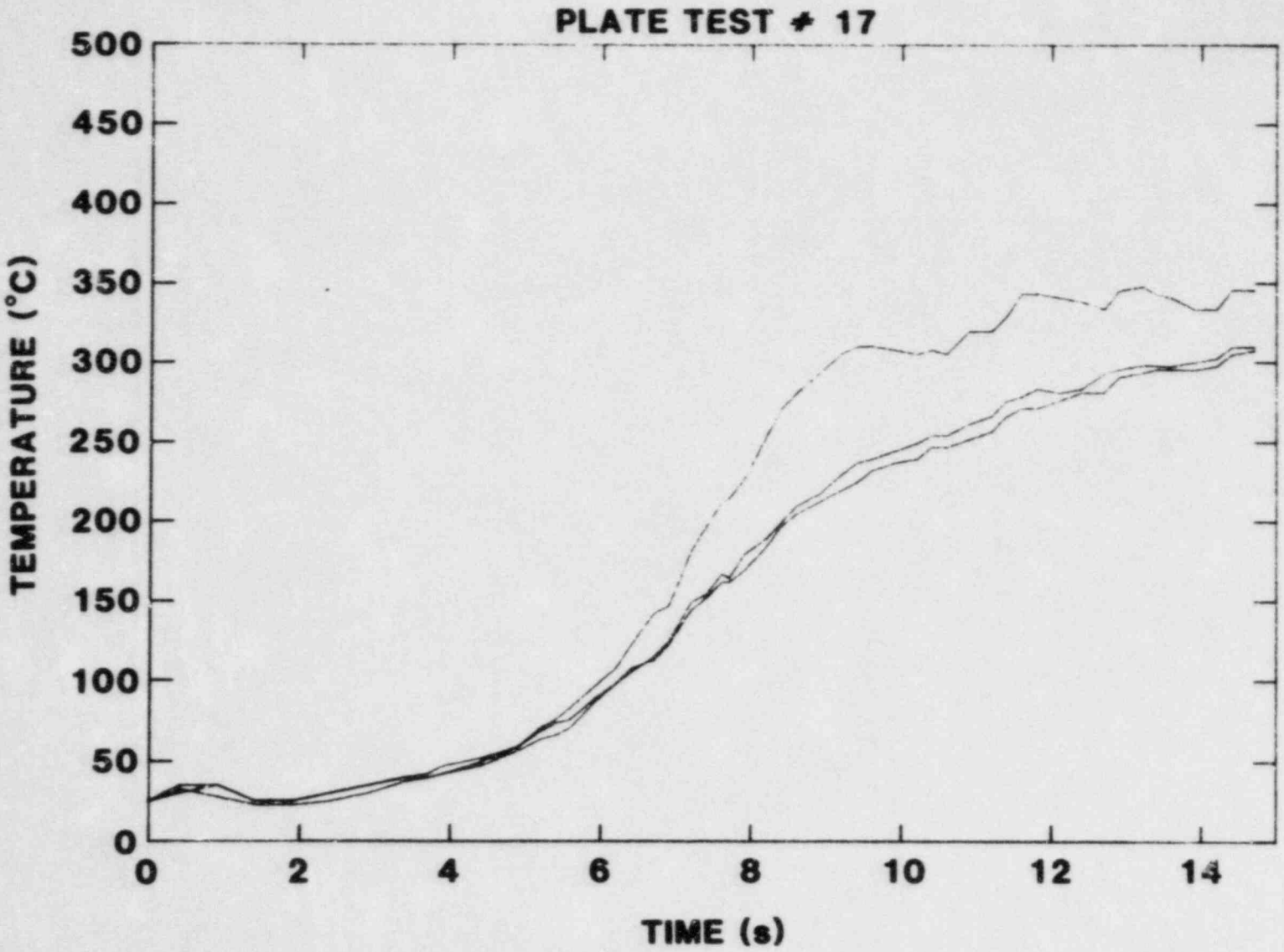

Figure B-11. Temperature Data from Test PLATE #17.

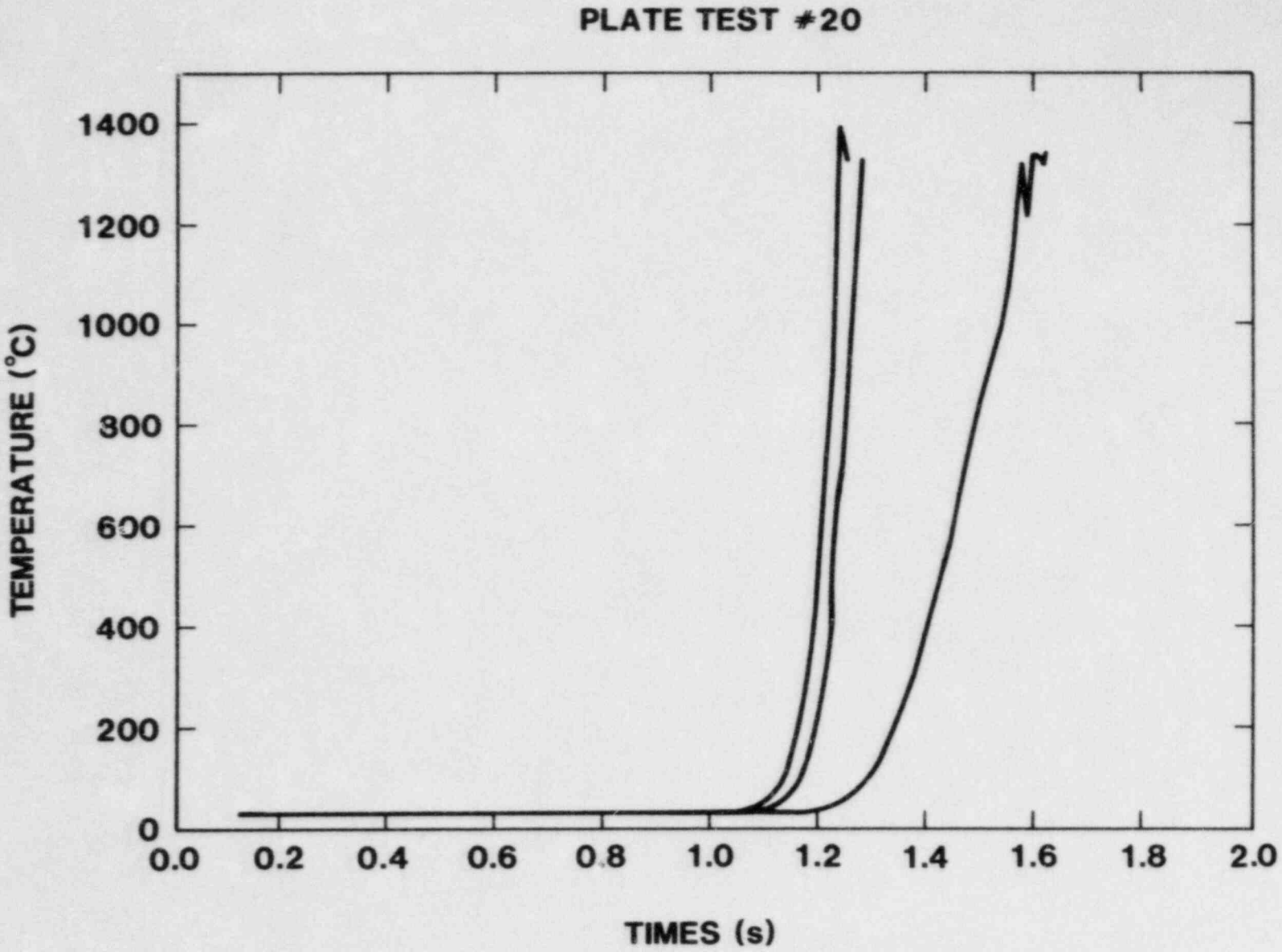

Figure B-12. Temperature Data from Test PLATE #20.

APPENDIX C

Description of Inverse Heat Conduction Analysis

The inverse heat conduction problem consists of using temperature data to derive the boundary condition for a heated body. The differential equation that describes the physics of heating a finite slab is:

$$\rho C(T) \frac{\partial T}{\partial t} = \frac{\partial}{\partial X} K(T) \frac{\partial T}{\partial X}$$

subject to the boundary conditions:

$$-K\frac{dT}{dx}\Big|_{x=0} = Q(t) \text{ for } t>0$$

$$-K\frac{dT}{dx}\Big|_{x=L} = 0 \text{ for } t>0$$

where L is the slab thickness. The initial condition is

$$T(x) = f(x) \text{ for } t=0 \text{ and } 0 \leq x \leq L$$

For the analyses done here f(x) is assumed constant for all x such that $0 \leq x \leq L$.

The solution of this differential equation when the boundary and initial conditions are known is well-established though the solution must be obtained numerically for even modestly complicated situations such as those that involve temperature dependent thermal properties, K(T) and C(T). The inverse problem is, however, ill-posed in the sense that the derived boundary condition is not a smooth function of the temperature data (1). The inverse problem is not catastrophically ill-posed so that with sufficient care the boundary

condition can be derived from temperature data. The ill-posed nature of the problem does place a strong limit on the time resolution that can be achieved in the solution (1).

Techniques for solving the inverse problem are under active study. Beck (2) has found that a non-linear least squares solution method will work. By this method the quantity S^2 is minimized where

$$S^2 = \sum_{i=1}^{N} \sum_{j=1}^{R} (Y_{i,j} - T_{i,j})^2$$

and

N = number of points within the slab for which temperature data are obtained

R = number of temperature data points in time used (so called "future" points).

$Y_{i,j}$ = temperature observed at the i^{th} location and j^{th} time point

$T_{i,j}$ = calculated temperature at the i^{th} location and j^{th} time point.

The calculated temperatures, $T_{i,j}$, are functions of the boundary condition. S^2 is minimized with respect to the boundary condition.

Beck assumes that the heat flux at the boundary is piecewise constant. It was found in this work that the piecewise constant assumption limited the accuracy and resolution of the solution. The piecewise constant assumption could be used to obtain a good first approximation to the heat flux at the boundary. Once this first approximation was obtained, the problem could then be solved again using the temporal variation in the boundary condition derived from the first approximation. The effectiveness of this method was demonstrated by solution of the triangular heat flux problem Beck solved in first presenting his approach to the inverse heat flux problem. Calculated and assumed heat fluxes are collected in Table C-1. A single iteration substantially improves the calculated heat flux. After eight iterations the differences between the calculated and assumed heat fluxes are significant only at the peak of the triangle where there is a non-differentiable point in the heat flux.

The "exact" temperature data used to demonstrate the inverse heat flux calculation are of considerable aid in obtaining a correct solution. Beck examined the effects of random noise and truncation of the data on the derived heat flux. Random noise will not greatly degrade the performance of a least-squares procedure provided the number of data points is large enough. Temperature data collected in an experiment are not subject to purely random noise. More typical errors arise because a temperature signal must change by a finite amount before the data acquisition system registers a change. Truncation of the data to a finite accuracy is also a source of error especially with digital data acquisition equipment.

To test the performance of the inverse heat flux calculation method, "exact" data were treated by a filter that:

(1) introduced $\pm$2% random errors in the data

(2) registered a change in temperature only when a data point differed by 1% of the maximum temperature in the problem from the previous data point

(3) truncated the data to three digits.

This was a harsh treatment of the temperature data but one that gives a fair representation of the quality of data likely to be obtained in the PLATE experiments.

The heat fluxes derived from the filtered data are shown in Figure C-1. These results were obtained with four iterations of the least-squares procedure. Quite clearly there is significant scatter in the derived heat flux values. The scattered values do cluster around the actual heat flux and do reproduce the global features of the time variation in heat flux. They give a fair indication of how much significance should be attached to variations in derived heat fluxes from point-to-point in an actual problem.

The derivation of heat fluxes from temperature data obtained in tests PLATE #15 and PLATE #17 was done as follows:

(1) the problem was formulated as a finite slab of thickness 0.95 cm heated on one face by a time dependent heat flux and insulated on the other face.

(2) The initial temperature of the slab was assumed constant at 25^{o}C.

Table C-1. Comparison of Calculated and Actual Surface Heat Fluxes

TIME	SURFACE HEAT FLUX				
(s)	ACTUAL	ITERATION 1	ITERATION 2	ITERATION 4	ITERATION 8
0	0	0.0302	0.0065	0.0019	5.4×10^{-5}
0.04	0.04	0.0608	0.0408	0.0409	0.0400
0.08	0.08	0.1028	0.0788	0.0803	0.0800
0.12	0.12	0.1453	0.1200	0.1201	0.1200
0.16	0.16	0.1856	0.1602	0.1602	0.1600
0.20	0.20	0.2251	0.1999	0.2001	0.2000
0.24	0.24	0.2649	0.2399	0.2399	0.2400
0.28	0.28	0.3049	0.2800	0.2800	0.2800
0.32	0.32	0.3450	0.3200	0.3200	0.3200
0.36	0.36	0.3850	0.3600	0.3600	0.3600
0.40	0.40	0.4250	0.4000	0.4002	0.4000
0.44	0.44	0.4650	0.4400	0.4404	0.4400
0.48	0.48	0.5050	0.4805	0.4801	0.4798
0.52	0.52	0.5448	0.5244	0.5203	0.5205
0.56	0.56	0.5769	0.5696	0.5610	0.5617
0.60	0.60	0.5767	0.5871	0.5784	0.5788
0.64	0.56	0.5424	0.5639	0.5585	0.5586
0.68	0.52	0.4967	0.5215	0.5186	0.5186
0.72	0.48	0.4538	0.4792	0.4776	0.4776
0.76	0.44	0.4142	0.4397	0.4393	0.4391
0.80	0.40	0.3750	0.4002	0.4004	0.4002
0.84	0.36	0.3352	0.3601	0.3603	0.3602
0.88	0.32	0.2950	0.3199	0.3200	0.3159
0.92	0.28	0.2550	0.2799	0.2799	0.2799
0.96	0.24	0.2150	0.2400	0.2400	0.2400
1.00	0.20	0.1750	0.2000	0.2000	0.2000
1.04	0.16	0.1350	0.1600	0.1600	0.1600
1.08	0.12	0.0950	0.1200	0.1200	0.1200
1.12	0.08	0.0550	0.0800	0.0800	0.0800
1.16	0.04	0.0150	0.0400	0.0400	0.0400
1.20	0	-0.0250	3.07×10^{-6}	1.5×10^{-5}	4.4×10^{-5}

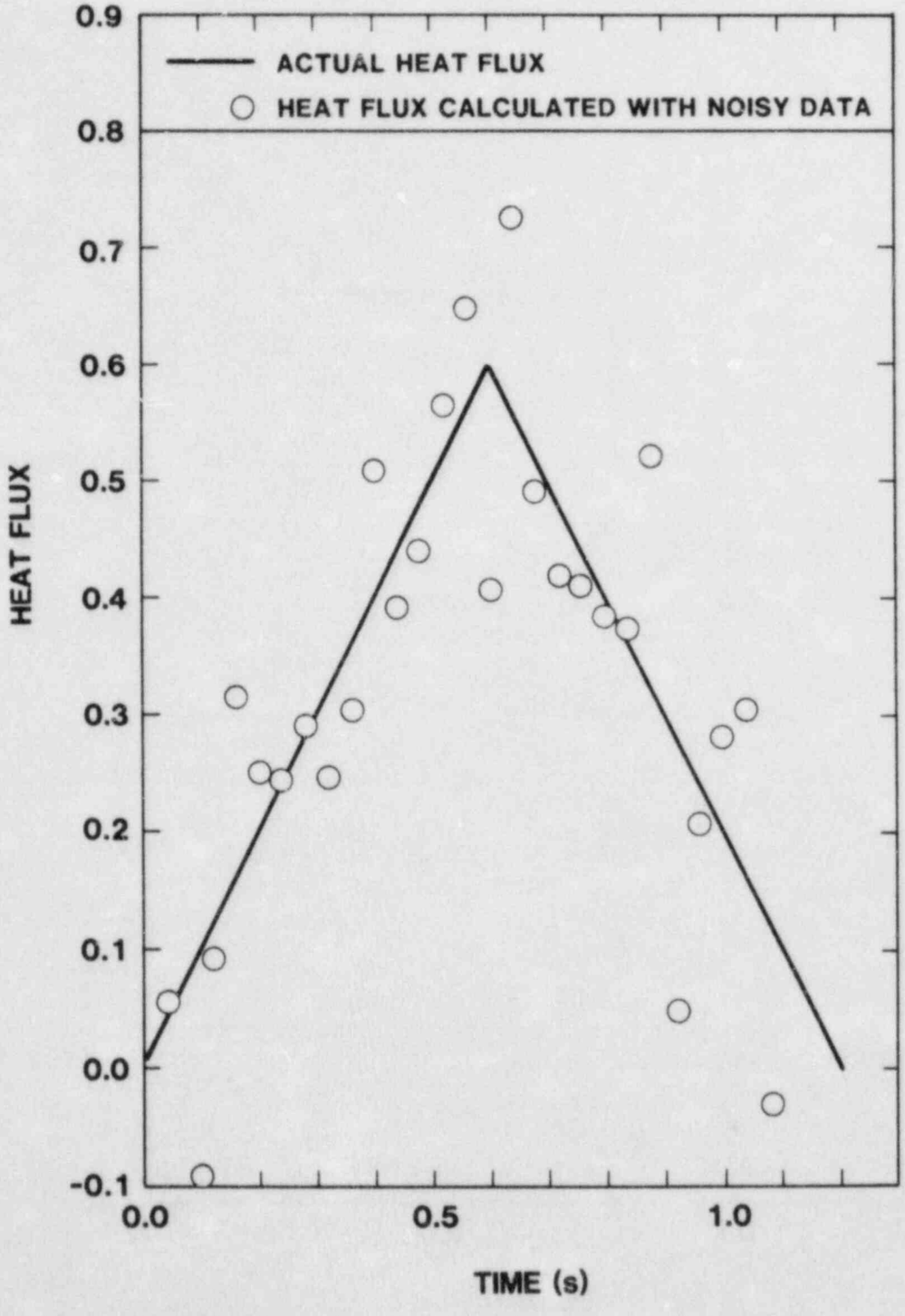

Figure C-1. Calculated Heat Flux Based on "Noisy", "Filtered" Data.

(3) The thermal conductivity, heat capacity, and density of the slab material varied with temperature as described in reference 3.

(4) Temperature data for the insulated face of the slab were available at 0.30 s time intervals.

(5) Sixteen future temperatures were used.

(6) Temperature calculations were made with a Crank-Nicholson scheme modified as described in reference 3 to account for temperature dependence of the thermal properties.

(7) The time step of the temperature calculations was 0.1 s and the spacial nodalization of the slab was 0.05 cm.

(8) The oxide coatings on the plates were ignored except insofar as they changed the problem from one with a temperature condition to a problem with a heat flux boundary condition.

The assumptions embodied in this approach to the problem are all non-controversal except the first. In test PLATE #15 a pool of melt was collected. Very quickly then the heat flux to the plate could be assumed uniform at least over broad enough an area that temperature data on the unexposed face of the plate would not be affected by deviations from this assumption. On the other hand, melt was deliberately drained off the plate in test PLATE #17. In this case the predominant heat flux to the plate was directed over a local area somewhat larger than the stream diameter (2 cm). It is not immediately obvious that this two-dimensional situation is well-approximated as a one dimensional problem of a uniformly exposed slab.

Some indication of the magnitude of possible errors caused by the one dimensional assumption in the treatment of test PLATE #17 may be gained by comparing analytic solutions for an analogous situation involving a semi-infinite body with constant thermophysical properties and a constant heat flux. The temperature distribution in such a body when the free surface is exposed to a uniform, constant heat flux, Q, is:

$$T(x,t) = T_c + \frac{2Q}{K}\left\{\left(\frac{\alpha t}{\pi}\right)^{1/2}\exp(-x^2/4\alpha t) - \frac{x}{2}\operatorname{erfc}\left(\frac{x}{2\sqrt{\alpha t}}\right)\right\}$$

where

K is the thermal conductivity and α is the diffusivity.

When the heat flux to the free surface is confined to a circular region of radius R, the temperature distribution in the body, T(r,x,t), is given by:

$$T(r,x,t) = T_o + \frac{RQ}{2K} \int_0^\infty J_o(\lambda r) J_1(2R) \{\lambda f(\lambda)/\lambda\} \, d_\lambda$$

where

$$f(\lambda) = \exp(-\lambda x)\operatorname{erfc}\left[\frac{x}{2\sqrt{\alpha t}} - \lambda\sqrt{\alpha t}\right] - \exp(\lambda x)\operatorname{erfc}\left[\frac{x}{2\sqrt{\alpha t}} + \lambda\sqrt{\alpha t}\right]$$

$J_o(x)$ and $J_1(x)$ are the first and second order Bessel functions of the first kind. Thus, at locations on the axis, r=0, temperatures are given by:

$$T(o,x,t) - T_o = \frac{2Q\sqrt{\alpha t}}{K} \left\{ \operatorname{ierfc} \frac{x}{2\sqrt{\alpha t}} - \operatorname{ierfc}\left[\frac{(x^2 + R^2)^{1/2}}{2\sqrt{\alpha t}}\right] \right\}$$

where

$$\operatorname{ierfc}(x) = \frac{1}{\sqrt{\pi}} \exp(-x^2) - x\operatorname{erfc}(x)$$

The temperatures within the body exposed to heat flux over a finite circle are always smaller than temperatures within a body exposed to a uniform temperature. The relative difference between temperatures within the semi-infinite bodies in these two cases is given by:

$$\varepsilon(x,t) = \frac{\text{ierfc}\left[\frac{(x^2 + R^2)^{1/2}}{2\sqrt{\alpha t}}\right]}{\text{ierfc}\left(\frac{x}{2\sqrt{\alpha t}}\right)} = \frac{T(x,t) - T(r=o,x,t)}{T(x,t)}$$

which is independent of the heat flux.

The value of $\varepsilon(0.95,t)$ for the case R=2 and $\alpha = 0.11$, is plotted against time in Figure C-2. These results show that errors are negligible (< 1%) up to a time of about 3 seconds. Between 3 seconds and 6.5 seconds the relative error increases to about 10%. This error is still tolerable if only order-of-magnitude results are sought. Beyond about 7 seconds the error associated with the one-dimensional approximation becomes intolerable.

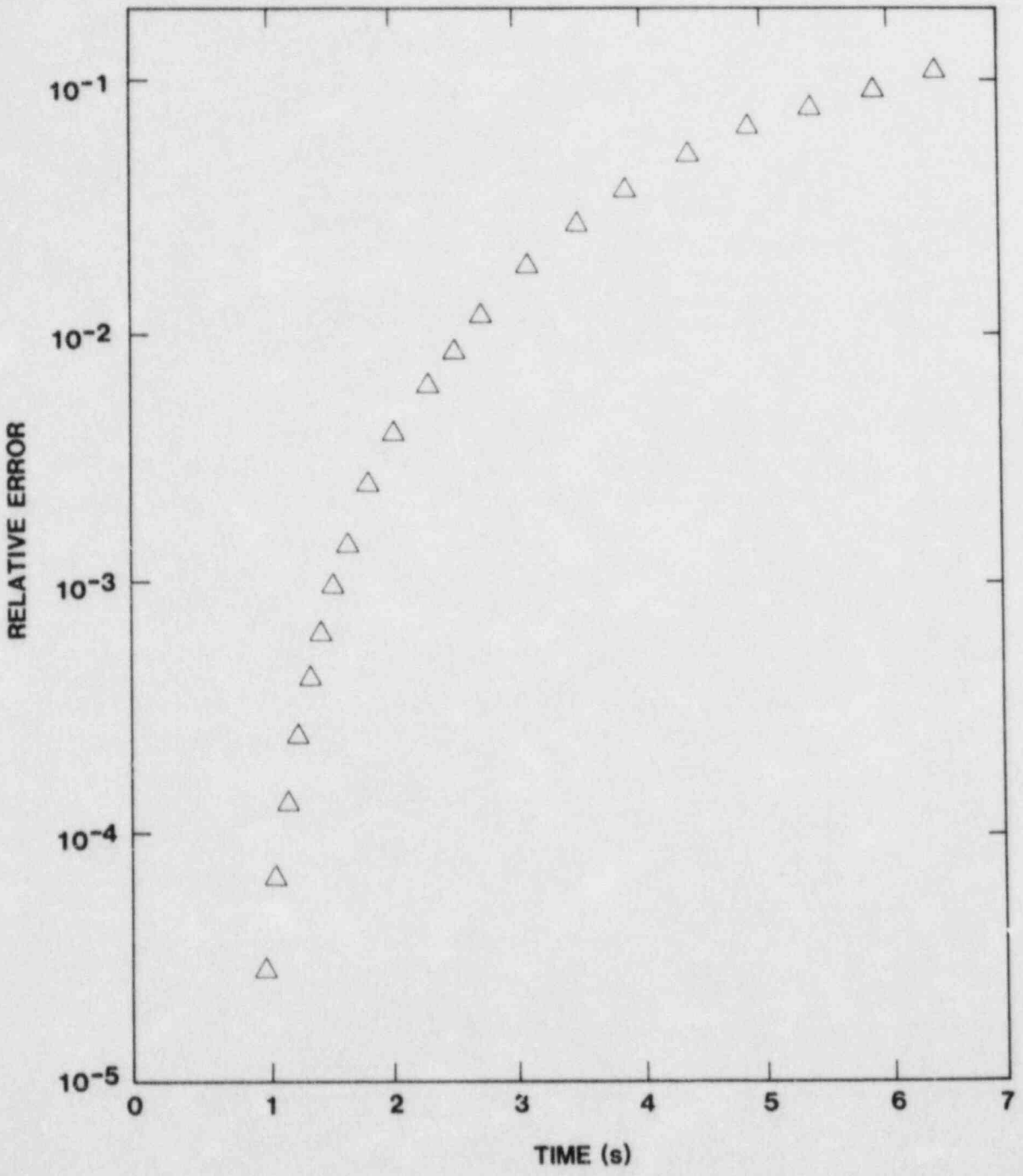

Figure C-2. Time Dependence of the Relative Temperature Error Associated with the One-Dimensional Approximation.

References

(1) C. F. Weber, Int. J. Heat Mass Transfer 24 1783 (1981).

(2) J. V. Beck, Int. J. Heat Mass Transfer 13 703-716 (1970).

(3) D. A. Powers and F. E. Arellano, Erosion of Steel Structures by High Temperature Melts, NUREG/CR-2284; SAND81-1755, Sandia National Laboratories, Albuquerque, NM, 87185.

DISTRIBUTION:

U.S. NRC Distribution Contractor (CDSI) (275 copies)
7300 Pearl Street
Bethesda, MD 20014
275 copies for R3

U.S. Nuclear Regulatory Commission (16)
Office of Nuclear Regulatory Research
Washington, DC 20555
Attn: O. E. Bassett
B. S. Burson
R. T. Curtis
C. N. Kelber
J. Larkins
T. Lee (5)
M. Silberberg
R. W. Wright
T. Walker
W. Pasedag

U.S. Nuclear Regulatory Commission (4)
Office of Nuclear Regulatory Regulation
Washington, DC 20555
Attn: L. G. Hulman
P. Easky
J. Rosenthal
J. Mitchell

U.S. Department of Energy (2)
Albuquerque Operations Office
P. O. Box 5400
Albuquerque, NM 87185
Attn: J. R. Roeder, Director
Operational Safety Division
D. K. Nowlin, Director
Special Programs Division
For: C. B. Quinn
D. Plymale

U.S. Department of Energy
Office of Nuclear Safety Coordination
Washington, DC 20545
Attn: R. W. Barber

Electric Power Research Institute
3412 Hillview Avenue
Palo Alto, CA 94303
Attn: R. Vogel
R. Sehgal

Professor T. Theofanous
Purdue University
School of Engineering
West Lafayette, IN 47907

Dr. R. Henry
Fauske & Associates
16W070 West 83rd Street
Burr-Ridge, IL 60521

M. L. Corradini
Nuclear Engineering Dept.
University of Wisconsin
Madison, WI 53706

I. Catton
UCLA
Nuclear Energy Laboratory
405 Hilgard Avenue
Los Angeles, CA 90024

Brookhaven National Laboratory (4)
Department of Nuclear Energy
Building 820
Upton, NY 11973
Attn: R. A. Bari
T. Pratt
G. Greene
T. Ginsberg

Professor R. Seale
Department of Nuclear Engineering
University of Arizona
Tucson, AZ 85721

Oak Ridge National Laboratory (2)
P. O. Box Y
Oak Ridge, TN 37830
Attn: T. Kress
S. Hodge

K. Holtzclaw
General Electric - San Jose
Mail Code 682
175 Kurtner Avenue
San Jose, CA 95125

Argonne National Laboratory
9700 S. Cass Avenue
Argonne, IL 60439
Attn: D. Pedersen

Cathy Anderson
Nuclear Safety Oversight Commission
1133 15th St., NW
Room 307
Washington, DC 20005

Battelle Columbus Laboratory (3)
505 King Avenue
Columbus, OH 43201
Attn: P. Cybulskis
R. Denning
J. Gieseke

J. E. Antill
Berkeley Nuclear Laboratory
Berkeley GL 139 PB
Gluocestershire
United Kingdom

W. G. Cunliffe
Bldg. 396
British Nuclear Fuels, Ltd.
Springfields Works
Salwick, Preston
Lancs
United Kingdom

Reactor Development Division (4)
UKAEA - Atomic Energy Establishment
Winfrith, Dorchester
Dorset
United Kingdom
Attn: R. G. Tyror, Head
T. Briggs
R. Potter
A. Nichols

Projekt Nucleare Sicherheit (3)
Kerforschungszentrum Karlsruhe
Postfach 3640
75 Karlsruhe
Federal Republic of Germany
Attn: J. P. Hoseman
Albrecht
H. H. Rininsland

Mr. G. Petrangeli
Direzione Centrale della Srcurezza
Nucleare e della Protezione Sanitaria (DISP)
Entre Nazionnle Energie Alternative (ENEA)
Vrale Regina Margherita, 125
Casella Postale N. 2358
I-00100 Roma A.D., ITALY

Dr. K. J. Brinkman
Reactor Centrum Nederland
P.O. Box 1
1755 ZG Petten
THE NETHERLANDS

Mr. H. Bairiot, Chief
Department LWR Fuel
Belgonucleaire
Rue de Champde Mars. 25
B-1050 BRUSSELS, BELGIUM

Dr. S. Saito
Japan Atomic Energy Research Institute
Takai Research Establishment
Tokai-Mura, Naku-Gun
Ibaraki-ken
JAPAN

Wang Lu
TVA
400 Commerce, W9C157-CK
Knoxville, TN 37902

M. Fontana
Director, IDCOR Program
Technology for Energy, Inc.
P. O. Box 22996
10770 Dutchtown Rd.
Knoxville, TN 37922

H. J. Teague (3)
UKAEA
Safety and Reliability Directorate
Wigshaw Lane
Culcheth
Warrington, WA3 4NE
United Kingdom

Dr. Fran Reusenbach
Gesellschaft fur Reaktorsicherheit (GRS mbH)
Postfach 101650
Glockengasse 2
5000 Koeln 1
Federal Republic of Germany

3141 C. M. Ostrander (5)
3151 W. L. Garner (1)
6000 E. H. Beckner
6400 A. W. Snyder
6410 J. W. Hickman
6420 J. V. Walker
6420 J. B. Rivard
6421 T. R. Schmidt
6422 D. A. Powers (5)
6422 F. E. Arellano (5)
6422 J. E. Brockmann
6422 R. M. Elrick
6422 E. R. Copus
6422 J. E. Gronager
6422 T. M. Kerley
6422 D. A. Lucero
6422 A. L. Ouellette, Jr.

6422	E. Randich
6422	A. R. Taig
6423	P. S. Pickard
6425	D. R. Bradley
6425	W. J. Camp
6425	M. Pilch
6425	A. Suo Anttila
6425	W. Frid
6427	M. Berman
6440	D. A. Dahlgren
6442	W. A. Von Riesemann
6449	K. D. Bergeron
6450	J. A. Reuscher
6454	G. L. Cano
7530	T. B. Lane
7537	N. R. Keltner
7537	T. Y. Chu
7537	R. U. Acton
7537	B. F. Blackwell
8424	M. A. Pound

NRC FORM 335 (7-77)

BIBLIOGRAPHIC DATA SHEET

NUREG/CR-3366
SAND83-1350

2 TITLE AND SUBTITLE

High Temperature Melt Attack on Steel and Urania-Coated Steel

3 LEAVE BLANK

4 RECIPIENT'S ACCESSION NUMBER

5 DATE REPORT COMPLETED

MONTH: December YEAR: 1983

6 AUTHOR(S)

D. A. Powers
F. E. Arellano

7 DATE REPORT ISSUED

MONTH: March YEAR: 1984

8 PERFORMING ORGANIZATION NAME AND MAILING ADDRESS (Include Zip Code)

Sandia National Laboratories
Albuquerque, NM 87185

9 PROJECT/TASK/WORK UNIT NUMBER

10 FIN NUMBER

NRC Fin. No. A1247

11 SPONSORING ORGANIZATION NAME AND MAILING ADDRESS (Include Zip Code)

Division of Accident Evaluation
Severe Accident Assessment Branch
U. S. Nuclear Regulatory Commission
Washington, DC 20555

12a TYPE OF REPORT

P7
Experimental Investigations

12b PERIOD COVERED (Inclusive dates)

13 SUPPLEMENTARY NOTES

14 ABSTRACT (200 words or less)

Corium and Thermitic melts were teemed at various velocities onto bare steel plates and steel plates coated with urania. An empirical correlation of the penetration data is developed.

15a KEY WORDS AND DOCUMENT ANALYSIS

15b DESCRIPTORS

Corium, Steel Erosion, Urania Coating, Thermite, Reactor Vessel

16 AVAILABILITY STATEMENT

unlimited

17 SECURITY CLASSIFICATION (This report)

Unclassified

18 NUMBER OF PAGES

19 SECURITY CLASSIFICATION (This page)

Unclassified

20 PRICE

$

Org.	Bldg.	Name	Rec'd by	Org.	Bldg.	Name	Rec'd by

120555078877 1 1AN1R7
US NRC
ADM-DIV OF TIDC
POLICY & PUB MGT BR-PDR NUREG
W-501
WASHINGTON DC 20555

Sandia National Laboratories